

# 1           **Is the recovery of stratospheric O<sub>3</sub> speeding up in the Southern Hemisphere?**

## 2                           **An evaluation from the first IASI decadal record (2008-2017)**

3  
4 Catherine Wespes<sup>1</sup>, Daniel Hurtmans<sup>1</sup>, Simon Chabrillat<sup>2</sup>, Gaétane Ronsmans<sup>1</sup>, Cathy  
5 Clerbaux<sup>3,1</sup> and Pierre-François Coheur<sup>1</sup>

6 <sup>1</sup>Université Libre de Bruxelles (ULB), Faculté des Sciences, Chimie Quantique et  
7 Photophysique, Bruxelles, Belgique

8 <sup>2</sup>Belgian Institute for Space Aeronomy, Brussels, Belgium

9 <sup>3</sup>LATMOS/IPSL, Sorbonne Université, UVSQ, CNRS, Paris, France

### 10 11 **Abstract**

12 In this paper, we present the global fingerprint of recent changes in the mid-upper stratospheric  
13 (MUS<sub>t</sub>; <25hPa) ozone (O<sub>3</sub>) in comparison with the lower stratospheric (LSt; 150-25 hPa) O<sub>3</sub>  
14 derived from the first 10 years of the IASI/Metop-A satellite measurements (January 2008 –  
15 December 2017). The IASI instrument provides vertically-resolved O<sub>3</sub> profiles with very high  
16 spatial and temporal (twice daily) samplings, allowing to monitor O<sub>3</sub> changes in these two  
17 regions of the stratosphere. By applying multivariate regression models with adapted geophysical  
18 proxies on daily mean O<sub>3</sub> time series, we discriminate anthropogenic trends from various modes  
19 of natural variability, such as the El Niño/Southern Oscillation – ENSO. The representativeness  
20 of the O<sub>3</sub> response to its natural drivers is first examined. One important finding relies on a  
21 pronounced contrast between a positive LSt O<sub>3</sub> response to ENSO in the extra-tropics and a  
22 negative one in the tropics, with a delay of 3 months, which supports a stratospheric pathway for  
23 the ENSO influence on lower stratospheric and tropospheric O<sub>3</sub>. In terms of trends, we find an  
24 unequivocal O<sub>3</sub> recovery from the available period of measurements in winter/spring at mid-high  
25 latitudes for the two stratospheric layers sounded by IASI (>~35°N/S in the MUS<sub>t</sub> and >~45°S in  
26 the LSt) as well as in the total columns at southern latitudes (>~45°S) where the increase reaches  
27 its maximum. These results confirm the effectiveness of the Montreal protocol and its  
28 amendments, and represent the first detection of a significant recovery of O<sub>3</sub> concurrently in the  
29 lower, in the mid-upper stratosphere and in the total column from one single satellite dataset. A  
30 significant decline in O<sub>3</sub> at northern mid-latitudes in the LSt is also detected, especially in  
31 winter/spring of the northern hemisphere. Given counteracting trends in LSt and MUS<sub>t</sub> at these  
32 latitudes, the decline is not categorical in total O<sub>3</sub>. When freezing the regression coefficients  
33 determined for each natural driver over the whole IASI period but adjusting a trend, we calculate  
34 a significant speeding up in the O<sub>3</sub> response to the decline of O<sub>3</sub> depleting substances (ODS) in  
35 the total column, in the LSt and, to a lesser extent, in the MUS<sub>t</sub>, at high southern latitudes over  
36 the year. Results also show a small significant acceleration of the O<sub>3</sub> decline at northern mid-  
37 latitudes in the LSt and in the total column over the last years. That, specifically, needs urgent  
38 investigation for identifying its exact origin and apprehending its impact on climate change.

39 Additional years of IASI measurements would, however, be required to confirm the O<sub>3</sub> change  
40 rates observed in the stratospheric layers over the last years.

41

## 42 **1 Introduction**

43

44 Ozone is a key radiatively active gas of the Earth atmosphere, in both the troposphere and the  
45 stratosphere. While, in the troposphere, O<sub>3</sub> acts as a strong pollutant and an important  
46 greenhouse gas, in the stratosphere and, more particularly, in the middle-low stratosphere, it  
47 forms a protective layer for life on Earth against harmful solar radiation. In the 1980s, the  
48 scientific community motivated decision-makers to regulate the use of chlorofluorocarbons  
49 (CFCs), after the unexpected discovery of the springtime Antarctic ozone hole (Chubachi, 1984;  
50 Farman et al., 1985) that was suspected to be induced by continued use of CFCs (Molina and  
51 Rowland, 1974; Crutzen, 1974).<sup>2</sup> The O<sub>3</sub> depletion was later verified from measurements at other  
52 Antarctic sites (e.g. Farmer et al., 1987) and from satellite observations (Stolarski et al., 1986),  
53 and explained by the role of CFC's on the massive destruction of O<sub>3</sub> following heterogeneous  
54 reactions on the surface of polar stratospheric clouds (Solomon, 1986; 1999 and references  
55 therein). The world's nations reacted to that human-caused worldwide problem by ratifying the  
56 International Vienna Convention for the Protection of the Ozone Layer in 1985 and the Montreal  
57 Protocol in 1987 with its later amendments, which forced the progressive banning of these ozone  
58 depleting substances (ODS) in industrial applications by early 1990s with a total phase-out of the  
59 most harmful CFCs by the year 2000.

60

61 A recovery from O<sub>3</sub> depletion is expected in response to the Montreal Protocol and its  
62 amendments, but with a delayed period due to the long residence time of halocarbons in the  
63 atmosphere (Hofmann et al., 1997; Dhomse el al., 2006; WMO, 2007; 2011). The decline of  
64 CFCs in the stratosphere was only initiated about 10 years after their phasing out (Anderson et  
65 al., 2000; Newman et al., 2006; Solomon et al., 2006 ; Mäder et al., 2010; WMO, 2011; 2014).  
66 The early signs of ozone response to that decline were identified in several studies that reported  
67 first a slowdown in stratospheric ozone depletion (e.g. Newchurch et al., 2003; Yang et al.,  
68 2008), followed by a leveling off of upper stratospheric (e.g. WMO, 2007) and total O<sub>3</sub> (e.g.  
69 WMO, 2011; Shepherd et al., 2014) depletion since the 2000's. A significant onset of recovery  
70 was identified later for upper stratospheric O<sub>3</sub> (e.g. WMO, 2014; 2018; Harris et al., 2015). Only  
71 a few studies have shown evidence for increasing total column O<sub>3</sub> in polar regions during  
72 springtime (e.g. Salby et al., 2011; Kuttippurath et al., 2013; Shepherd et al., 2014; Solomon et  
73 al., 2016). Statistically significant long-term recovery in total O<sub>3</sub> column (TOC) on a global scale  
74 has not yet been observed, likely because of counteracting trends in the different vertical  
75 atmospheric layers. Ball et al. (2018) have found that a continuing O<sub>3</sub> decline prevails in the  
76 lower stratosphere since 1998, leading to a slower increase in total O<sub>3</sub> than expected from the  
77 effective equivalent stratospheric chlorine (EESC) decrease. However, the reported decline is not  
78 reproduced by the state-of-the-art models and its exact reasons are still unknown (Ball et al.,

79 2018). Wargan et al. (2018) and Galytska et al. (2019) recently reported that the decline in the  
80 extratropical lower stratosphere and tropical mid-stratosphere is dynamically controlled by  
81 variations in the tropical upwelling.

82  
83 Although recent papers based on observational datasets and statistical approaches agree that we  
84 currently progress towards an emergence into ozone recovery (e.g. Pawson et al., 2014; Harris et  
85 al., 2015; Steinbrecht et al., 2017; Sofieva et al., 2017; Ball et al., 2018; Weber et al., 2018),  
86 trend magnitude and trend significance over the whole stratosphere substantially differ from one  
87 study to another and, consequently, they are still subject to uncertainty (Keeble et al., 2018). A  
88 clear identification of the onset of O<sub>3</sub> recovery is very difficult due to concurrent sources of O<sub>3</sub>  
89 fluctuations (e.g. Reinsel et al., 2005; WMO, 2007, 2011). They include: changes in solar  
90 ultraviolet irradiance, in atmospheric circulation patterns such as the quasi-biennial oscillation  
91 (QBO; Baldwin et al., 2001) and the El Niño–Southern Oscillation (ENSO; e.g. Randel et al.,  
92 2009), in temperature, in ODS emissions and volcanic eruptions (e.g. Mt Pinatubo in 1991 and  
93 Calbuco in 2015) with their feedbacks on stratospheric temperature and dynamics (e.g. Jonsson  
94 et al., 2004). Furthermore, the differences in vertical/spatial resolution and in retrieval  
95 methodologies (inducing biases), possible instrumental degradations (inducing drifts), and use of  
96 merged datasets into composites, likely explain part of the trend divergence between various  
97 studies. ~~If Merging may be performed on deseasonalized anomalies, which offers the~~  
98 ~~advantage of removing instrumental biases between the individual data records (Sofieva et al.,~~  
99 ~~2017), but there remains large differences remain in anomaly values between the independent~~  
100 ~~datasets, as well as large instrumental drifts and drift uncertainty estimates that prevent deriving~~  
101 ~~statistically accurate trends (Harris et al., 2015; Hubert et al., 2016).~~

102  
103 In this context, there is a pressing need for long-duration, high-density and homogenized O<sub>3</sub>  
104 profile dataset to assess significant O<sub>3</sub> changes in different parts of the stratosphere and their  
105 contributions to the total O<sub>3</sub>.

106  
107 In this paper, we exploit the high frequency (daily) and spatial coverage of the IASI satellite  
108 dataset over the first decade of the mission (January 2008 – December 2017) to determine global  
109 patterns of reliable trends in the stratospheric O<sub>3</sub> records, separately in the Mid-Upper  
110 Stratosphere (MUS<sub>t</sub>) and the Lower Stratosphere (LS<sub>t</sub>). This study is built on previous analysis  
111 of stratospheric O<sub>3</sub> trends from IASI, estimated on latitudinal averages over a shorter period  
112 (2008-2013) (Wespes et al., 2016). A multivariate linear regression (MLR) model (annual and  
113 seasonal formulations) that is similar to that previously used for tropospheric O<sub>3</sub> studies from  
114 IASI (Wespes et al., 2017; 2018), but adapted here for the stratosphere with appropriate drivers,  
115 is applied to gridded daily mean O<sub>3</sub> time series in the MUS<sub>t</sub> and the LS<sub>t</sub>. The MLR model is  
116 evaluated in terms of its performance and its ability to capture the observed variability in Section  
117 2, in terms of representativeness of O<sub>3</sub> drivers in Section 3 and in terms of adjusted trends in  
118 Section 4. The minimum numbers of years of IASI measurements that is required to indeed

119 detect the adjusted trends from MLR in the two layers is also estimated in Section 4 that ends  
120 with an evaluation of the trends detectable in polar winter and spring and with an evaluation of a  
121 speeding up in the O<sub>3</sub> changes.

122

## 123 **2 Dataset and methodology**

124

### 125 **2.1 IASI O<sub>3</sub> data**

126

127 The Infrared Atmospheric Sounding Interferometer (IASI) is a nadir-viewing Fourier transform  
128 spectrometer designed to measure the thermal infrared emission of the Earth-atmosphere system  
129 between 645 and 2760 cm<sup>-1</sup>. Measurements are taken from the polar sun-synchronous orbiting  
130 meteorological Metop series of satellites, every 50 km along the track of the satellite at nadir and  
131 over a swath of 2200 km across track. With more than 14 orbits a day and a field of view of four  
132 simultaneous footprints of 12 km at nadir, IASI provides global coverage of the Earth twice a  
133 day at about 09:30 AM and PM mean local solar time.

134

135 The Metop program consists of a series of three identical satellites successively launched to  
136 ensure homogenous measurements of atmospheric parameters covering more than 15 years.  
137 Metop-A and -B have been successively launched in October 2006 and September 2012,  
138 respectively. The third and last satellite was launched in November 2018 onboard Metop-C. In  
139 addition to its exceptional spatio-temporal coverage, IASI also provides good spectral resolution  
140 and low radiometric noise, which allows the measurement of a series of gas-phase species and  
141 aerosols globally (e.g. Clerbaux et al., 2009; Hilton et al., 2012; Clarisse et al., 2018).

142

143 ~~For~~In this study, we use the O<sub>3</sub> profiles retrieved by the Fast Optimal Retrievals on Layers for  
144 IASI (FORLI-O<sub>3</sub>; version 20151001) near-real time processing chain set up at ULB (See  
145 Hurtmans et al, 2012 for a description of the retrieval parameters and the FORLI performances).  
146 The FORLI algorithm relies on a fast radiative transfer and a retrieval methodology based on the  
147 Optimal Estimation Method (Rodgers, 2000) that requires a priori information (a priori profile  
148 and associated variance-covariance matrix). The FORLI-O<sub>3</sub> a priori consists of one single profile  
149 and one covariance matrix built from the global Logan/Labow/McPeters climatology (McPeters  
150 et al., 2007). The profiles are retrieved on a uniform 1 km vertical grid on 41 layers from surface  
151 to 40 km with an extra layer from 40 km to the top of the atmosphere considered at 60 km.  
152 Previous characterization of the FORLI-O<sub>3</sub> profiles (Wespes et al., 2016) have demonstrated a  
153 good vertical sensitivity of IASI to the O<sub>3</sub> measurement with up to 4 independent levels of  
154 information on the vertical profile in the troposphere and the stratosphere (MUS<sub>t</sub>; LSt; upper  
155 troposphere-lower stratosphere – UTLS – 300-150 hPa; middle-low troposphere – MLT – below  
156 300 hPa). The two stratospheric layers that show distinctive patterns of O<sub>3</sub> distributions over the  
157 IASI decade (Fig. 1a) are characterized by high sensitivity (DOFS > 0.85; Fig. 1b) and low total  
158 retrieval errors (<5%; see Hurtmans et al., 2012; Wespes et al., 2016). The decorrelation between



159 the MUST and the LSt is further evidenced in Fig. 1d that shows low correlation coefficients (<  
160 0.4) between the mean absolute deseasonalized anomalies (as calculated in Wespes et al., 2017)  
161 in the two layers (Fig. 1c). Note that the highest correlation coefficients over the Antarctic (~0.4)  
162 are due to the smaller vertical sensitivity of the IASI measurements over cold surface (Clerbaux  
163 et al., 2009). The latest validation exercises for the FORLI-O<sub>3</sub> product have demonstrated a high  
164 degree of precision with excellent consistency between the measurements taken from the two  
165 IASI instruments on Metop-A and -B, as well as a good degree of accuracy with biases lower  
166 than 20% in the stratospheric layers (Boynard et al., 2018; Keppens et al. 2017). Thanks to these  
167 good IASI-FORLI performances, large-scale dynamical modes of O<sub>3</sub> variations and long-term O<sub>3</sub>  
168 changes can be differentiated in the four retrieved layers (Wespes et al., 2016). The recent  
169 validations have, however, reported a drift in the MUST FORLI-O<sub>3</sub> time series from comparison  
170 with O<sub>3</sub> sondes in the northern hemisphere (N.H.) ( $\sim 3.53 \pm 3.09$  DU.decade<sup>-1</sup> on average over  
171 2008–2016; Boynard et al., 2018) that was suggested to result from a pronounced discontinuity  
172 (“jump”) rather than from a progressive change. Further comparisons with CTM simulations  
173 from the Belgian Assimilation System for Chemical Observations (BASCOE; Chabrillat et al.,  
174 2018; Errera et al., 2019) confirm this jump that occurred on 15 September 2010 over all  
175 latitudes (see Fig. S1 of the supplementary materials). The discontinuity is suspected to result  
176 from updates in level-2 temperature data from Eumetsat that are used as inputs into FORLI (see  
177 Hurtmans et al., 2012). Hence, the apparent drift reported by Boynard et al. (2018) likely results  
178 from the jump rather than from a progressive “instrumental” drift. This is verified by the absence  
179 of drift in the O<sub>3</sub> time series after the jump (non-significant drift of  $-0.38 \pm 2.24$  DU.decade<sup>-1</sup> on  
180 average over October 2010 – May 2017; adapted from Boynard et al., 2018). This is in line with  
181 the excellent stability of the IASI Level-1 radiances over the full IASI period (Buffet et al.,  
182 2016). From the IASI-BASCOE comparisons, the amplitude of the jump has been estimated as  
183 lower than 2.0 DU in the 55°S–55°N latitude band and 4.0 DU in the 55°–90° latitude band of  
184 each hemisphere. The estimated amplitude of the jump is found to be relatively small in  
185 comparison to that of the decadal trends derived in Section 4, hence, it cannot explain the  
186 tendency-trend observed in the IASI dataset. Therefore, the jump is not taken into account in the  
187 MLR. The jump values will be, however, considered in the discussion of the O<sub>3</sub> trends (Section  
188 4).

189  
190 Finally, the present study only uses the daytime measurements (defined with a solar zenith angle  
191 to the sun < 83°) from the IASI-A (aboard Metop-A) instrument that fully covers the first decade  
192 of the IASI mission. The daytime measurements are characterized by a higher vertical sensitivity  
193 (e.g. Clerbaux et al., 2009). Quality flags developed in previous IASI studies (e.g. Boynard et al.,  
194 2018) were applied a posteriori to exclude data with a poor spectral fit, with less reliability or  
195 with cloud contamination.

## 196 197 **2.2 Multivariate regression model**

198

199 In an effort to unambiguously discriminate anthropogenic trends in O<sub>3</sub> levels from the various  
 200 modes of natural variability (illustrated globally in Fig.1c as deseasonalized anomalies), we have  
 201 applied to the 2.5°x2.5° gridded daily MUST and LSt O<sub>3</sub> time series, a MLR model that is similar  
 202 to that previously developed for tropospheric O<sub>3</sub> studies from IASI (see Wespes et al., 2017;  
 203 2018) but here adapted to fit the stratospheric variations:  
 204

$$205 \quad O_3(t) = Cst + x_{j=1} \cdot trend + \sum_{n=1:2} [a_n \cdot \cos(n\omega t) + b_n \cdot \sin(n\omega t)] + \sum_{j=2}^m x_j X_{norm,j}(t) + \varepsilon(t) \quad (1)$$

206  
 207 where  $t$  is the number of days,  $x_1$  is the trend coefficient in the data,  $\omega = 2\pi/365.25$ ,  $a_n, b_n, x_j$  are  
 208 the regression coefficients of the seasonal and non-seasonal variables and  $\varepsilon(t)$  is the residual  
 209 variation (assumed to be autoregressive with time lag of 1 day).  $X_{norm,j}$  are the  $m$  chosen  
 210 explanatory variables, commonly called “proxies”, which are normalized over the study period  
 211 (2008 – 2017) with:  
 212

$$213 \quad X_{norm}(t) = 2[X(t) - X_{median}] / [X_{max} - X_{min}] \quad (2)$$

214  
 215 In addition to harmonic terms that represent the 1-yr and 6-month variations, the MLR model  
 216 includes the anthropogenic O<sub>3</sub> response through a linear trend (LT) term and a set of proxies to  
 217 parameterize the geophysical processes influencing the abundance of O<sub>3</sub> in the stratosphere. The  
 218 MLR uses an iterative stepwise backward elimination approach to retain, at the end of the  
 219 iterations, the most relevant proxies (with a 95% confidence level) explaining the O<sub>3</sub> variations  
 220 (e.g. Mäder et al., 2007). Table 1 lists the selected proxies, their sources and their temporal  
 221 resolutions. The proxies describe the influence of the Quasi-Biennial Oscillation (QBO; visible  
 222 from the deseasonalized anomaly maps in Fig.1c with a typical band-like pattern around the  
 223 Equator) at 10 hPa and 30 hPa, of the North Atlantic and the Antarctic Oscillations (NAO and  
 224 AAO), of the El Niño/Southern Oscillation (ENSO), of the volcanic aerosols (AERO) injected  
 225 into the stratosphere, of the strength of the Brewer-Dobson circulation (BDC) with the Eliassen-  
 226 Palm flux (EPF), of the polar O<sub>3</sub> loss driven by the volume of polar stratospheric clouds (VPSC),  
 227 of the tropopause height variation with the geopotential height (GEO) and of the mixing of  
 228 tropospheric and stratospheric air masses with the potential vorticity (PV). The main proxies in  
 229 terms of their influence on O<sub>3</sub> are illustrated in Fig. 2 over the period of the IASI mission. The  
 230 construction of the EPF, VPSC and AERO proxies, which are specifically used in this study, is  
 231 explained hereafter, while the description of the other proxies can be found in previous IASI  
 232 studies (Wespes et al., 2016; [Wespes et al., 2017](#)).  
 233

234 The EPF proxy consists of the normalized upward component of the EP flux crossing 100 hPa  
 235 and spatially averaged over the 45°-75° latitude band for each hemisphere. The fluxes are

236 calculated from the NCEP/NCAR 2.5°x2.5° gridded daily reanalysis (Kalnay et al., 1996) over  
237 the IASI decade. The VPSC proxy is based on the potential volume of PSCs given by the volume  
238 of air below the formation temperature of nitric acid trihydrate (NAT) over 60°-90° north and  
239 south and calculated from the ERA-Interim reanalysis and from the MLS climatology of nitric  
240 acid (I. Wohltmann, private communication; Wohltmann et al., 2007; and references therein).  
241 The PSC volume is multiplied by the EESC to account for the changes in the amount of  
242 inorganic stratospheric chlorine that activates the polar ozone loss. The O<sub>3</sub> build-up and the polar  
243 O<sub>3</sub> loss are highly correlated with wintertime accumulated EP flux and PSC volume, respectively  
244 (Fusco and Salby, 1999; Randel et al., 2002; Fioletov and Shepherd, 2003 and Rex et al., 2004).  
245 These cumulative EP flux and PSC effects on O<sub>3</sub> levels are taken into account by integrating the  
246 EPF and VPSC proxies over time with a specific exponential decay time according to the  
247 formalism of Brunner et al. (2006; see Eq. 4). We set the relaxation time scale to 3 months  
248 everywhere, except during the wintertime build-up phase of O<sub>3</sub> in the extratropics (from October  
249 to March in the N.H. and from April to September in the southern hemisphere - S.H.) when it is  
250 set to 12 months. For EPF, it accounts for the slower relaxation time of extratropical O<sub>3</sub> in winter  
251 due to its longer photochemical lifetime. For VPSC, the 12-month relaxation time accounts for a  
252 stronger effect of stratospheric chlorine on spring O<sub>3</sub> levels: the maximum of the accumulated  
253 VPSC (Fig. 2) coincides with the maximum extent of O<sub>3</sub> hole that develops during springtime  
254 and that lasts until November. Note that correlations between VPSC and EPF are possible since  
255 the same method is used to build these cumulative proxies. VPSC and EPF are also dynamically  
256 anti-correlated to some extent since a strong BDC is connected with warm polar stratospheric  
257 temperatures and, hence, reduced PSC volume (e.g. Wohltmann et al., 2007).

258  
259 The AERO proxy is derived from aerosol optical depth (AOD) of sulfuric acid only. That proxy  
260 consists of latitudinally averaged (22.5°N-90°N – AERO-N, 22.5°S-90°S – AERO-S and 22.5°S-  
261 22.5°N – AERO-Eq) extinction coefficients at 12 μm calculated from merged aerosol datasets  
262 (SAGE, SAM, CALIPSO, OSIRIS, 2D-model-simulation and Photometer; Thomason et al.,  
263 2018) and vertically integrated over the two IASI stratospheric O<sub>3</sub> columns (AERO-MUSt and  
264 AERO-LSt). Fig.2 shows the AERO proxies (AERO-N, AERO-S and AERO-Eq) corresponding  
265 to the AOD over the whole stratosphere (150-2 hPa), while Fig.3 represents the latitudinal  
266 distribution of the volcanic sulfuric acid extinction coefficients integrated over the whole  
267 stratosphere (top panel) and, separately, over the MUSt (middle panel) and the LSt (bottom  
268 panel) from 2005 to 2017. The AOD distributions indicate the need for considering one specific  
269 AERO proxy for each latitudinal band (AERO-N, AERO-S and AERO-Eq) and for each vertical  
270 layer (AERO-MUSt and AERO-LSt). Note that, as an alternative proxy to AERO, the surface  
271 area density of ambient aerosol, that represents the aerosol surface available for chemical  
272 reactions, has been tested, giving similar results.

273  
274 Note also that, similarly to what has already been found for tropospheric O<sub>3</sub> from IASI (Wespes  
275 et al., 2016), several time-lags for ENSO (1-, 3- and 5-month lags; namely, ENSO-lag1, ENSO-

276 lag3 and ENSO-lag5) are also included in the MLR model to account for a possible delay in the  
277 O<sub>3</sub> response to ENSO at high latitudes.

278

279 Finally, autocorrelation in the noise residual  $\varepsilon(t)$  (see Eq. 1 in Wespes et al., 2016) is accounted  
280 for in the MLR analysis with time lag of one day to yield the correct estimated standard errors  
281 for the regression coefficients. They are estimated from the covariance matrix of the regression  
282 coefficients and corrected at the end of the iterative process by the autocorrelation of the noise  
283 residual. The regression coefficients are considered significant if they fall in the 95% confidence  
284 level (defined by  $2\sigma$  level).

285

286 In the seasonal formulation of the MLR model, the main proxies ( $x_j X_{norm,j}$ ; with  $x_j$ , the  
287 regression coefficient and  $X_{norm,j}$ , the normalized proxy) are split into four seasonal functions  
288 ( $x_{spr} X_{norm,spr} + x_{sum} X_{norm,sum} + x_{fall} X_{norm,fall} + x_{wint} X_{norm,wint}$ ) that are independently and  
289 simultaneously adjusted for each grid cell (Wespes et al., 2017). Hence, the seasonal MLR  
290 adjusts 4 coefficients (instead of one in the annual MLR) to account for the seasonal O<sub>3</sub> response  
291 to changes in the proxy. If that method avoids to over-constrain the adjustment by the year-round  
292 proxies and, hence, reduces the systematic errors, the smaller daily data points covered by the  
293 seasonal proxies translate to a lower significance of these proxies. This is particularly true for  
294 EPF and VPSC that compensate each other by construction. As a consequence, the annual MLR  
295 is performed first in this study and, then, complemented with the seasonal one when it is found  
296 helpful for further interpreting the observations.

297

298 Figure 4 shows the latitudinal distributions of the O<sub>3</sub> columns in the two stratospheric layers over  
299 the IASI decade (first panels in Fig.4 a and b), as well as those simulated by the annual MLR  
300 regression model (second panels) along with the regression residuals (third panels). The root  
301 mean square error (*RMSE*) of the regression residual and the contribution of the MLR model into

302 the IASI O<sub>3</sub> variations (calculated as  $\frac{\sigma(O_3^{\text{Fitted\_model}}(t))}{\sigma(O_3(t))}$  where  $\sigma$  is the standard deviation relative

303 to the regression model and to the IASI time series; bottom panels) are also represented (bottom  
304 panels). The results indicate that the model reproduces ~25-85% and ~35-95% of the daily O<sub>3</sub>  
305 variations captured by IASI in the MUST and the LSt, respectively, with the best representation  
306 in the tropics and the worst around the S.H. polar vortex, and that the residual errors are  
307 generally lower than 10% everywhere for the two layers, except for the spring O<sub>3</sub> hole region in  
308 the LSt. The *RMSE* relative to the IASI O<sub>3</sub> time series are lower than 15 DU and 20 DU at global  
309 scale in the MUST and the LSt, respectively, except around the S.H. polar vortex in the LSt (~30  
310 DU). On a seasonal basis (figure not shown), the results are only slightly improved: the model  
311 explains from ~35-90% and ~45-95% of the annual variations and the *RMSE* are lower than ~12  
312 DU and ~23 DU everywhere, in the MUST and the LSt, respectively. These results verify that the

313 MLR models (annual and seasonal) reproduce well the time evolution of O<sub>3</sub> over the IASI  
314 decade in the two stratospheric layers and, hence, that they can be used to identify and quantify  
315 the main O<sub>3</sub> drivers in these two layers (see Section 3).

316  
317 The MLR model has also been tested on nighttime FORLI-O<sub>3</sub> measurements only and  
318 simultaneously with daytime measurements, but this resulted in a lower quality fit, especially in  
319 the MUST over the polar regions. This is due to the smaller vertical sensitivity of IASI during  
320 nighttime measurements, especially over cold surface, which causes larger correlations between  
321 stratospheric and tropospheric layers (e.g. 40-60% at high northern latitudes versus ~10-20% for  
322 daytime measurements based on deseasonalized anomalies) and, hence, which mixes  
323 counteracting processes from these two layers. For this reason, only the results for the MLR  
324 performed on daytime measurements are presented ~~and discussed~~ in this paper.

325

### 326 **3 Drivers of O<sub>3</sub> natural variations**

327

328 Ascribing a recovery in stratospheric O<sub>3</sub> to a decline in stratospheric halogen species requires  
329 first identifying and quantifying natural cycles that may produce trend-like segments in the O<sub>3</sub>  
330 time series, in order to prevent any misinterpretation of those segments as signs of O<sub>3</sub> recovery.  
331 The MLR analysis performed in Section 2.2 that was found to give a good representation of the  
332 MUST and LSt O<sub>3</sub> records shows distinctive relevant patterns for the individual proxies retained  
333 in the regression procedure, as represented in Fig. 5. The fitted drivers are characterized by  
334 significant regional differences in their regression coefficients with regions of in-phase relation  
335 (positive coefficients) or out-of-phase relation (negative coefficients) with respect to the IASI  
336 stratospheric O<sub>3</sub> anomalies. The areas of significant drivers (in the 95% confidence limit) are  
337 surrounded by non-significant cells when accounting for the autocorrelation in the noise residual.  
338 Figures 6 a and b<sub>2</sub> respectively, represent the latitudinal averages of the fitted regression  
339 coefficients for the significant proxies showing latitudinal variation only in the O<sub>3</sub> response  
340 (namely, QBO, EPF, VPSC, AERO and ENSO) and of the contribution of these drivers into the  
341 O<sub>3</sub> variability (calculated as the product of the 2 $\sigma$  variability of each proxy by its corresponding  
342 fitted coefficient, i.e. the 2 $\sigma$  variability of the reconstructed proxies). The 2 $\sigma$  O<sub>3</sub> variability in the  
343 IASI measurements and in the fitted MLR model are also represented (black and grey lines,  
344 respectively). Figure 7 displays the same results as Fig. 6b but for the austral spring and winter  
345 periods only (using the seasonal MLR).

346

347 The PV and GEO proxies are generally minor components (not shown here) with relative  
348 contributions smaller than 10% and large standard errors (>80%), except in the tropics where the  
349 contribution for GEO reaches 40% in the LSt due to the tropopause height variation. Each other  
350 adjusted proxy (QBO, SF, EPF, VPSC, AERO, ENSO, NAO and AAO) is an important  
351 contributor to the O<sub>3</sub> variations, depending on the layer, region, and season as described next:

352

- 353 1. QBO - The QBO at 10hPa and 30hPa are important contributors around the Equator for  
354 the two stratospheric layers. It shows up as a typical band-like pattern of high positive  
355 coefficients confined equatorward of  $\sim 15^\circ\text{N/S}$  where the QBO is known to be a dominant  
356 dynamical modulation force associated ~~to with~~ strong convective anomalies (e.g. Randel  
357 and Wu, 1996; Tian et al., 2006; Witte et al., 2008). In that latitude band, QBO10 and  
358 QBO30 explain up to  $\sim 8$  DU and  $\sim 5$  DU, respectively, of the MUST and LSt yearly  $\text{O}_3$   
359 variations (see Fig. 5 and 6b; i.e. relative contributions up to  $\sim 50\%$  and  $\sim 40\%$  for  
360 QBO10/30 in MUST and LSt  $\text{O}_3$ , respectively). The QBO is also influencing  $\text{O}_3$  variations  
361 poleward of  $60^\circ\text{N/S}$  with a weaker correlation between  $\text{O}_3$  and equatorial wind anomalies  
362 as well as in the sub-tropics with an out-of-phase transition. That pole-to-pole QBO  
363 influence results from the QBO-modulation of extra-tropical waves and its interaction  
364 with the BDC (e.g. Fusco and Salby, 1999). A pronounced seasonal dependence is  
365 observed in the out-of-phase sub-tropical  $\text{O}_3$  anomalies in the MUST, with the highest  
366 amplitude oscillating between the hemispheres in their respective winter ( $\sim 5$  DU of  $\text{O}_3$   
367 variations explained by QBO10/30 at  $\sim 20^\circ\text{S}$  during JJA and at  $\sim 20^\circ\text{N}$  during DJF; see  
368 Fig. 7b for the JJA period in the MUST the DJF period is not shown), which is in  
369 agreement with Randel and Wu (1996). The amplitude of the QBO signal is found to be  
370 stronger for QBO30 than for QBO10 in the LSt, which is in good agreement with studies  
371 from other instruments for the total  $\text{O}_3$  (e.g. Baldwin et al., 2001; Steinbrecht et al., 2006;  
372 Frossard et al., 2013; Coldewey-Egbers et al., 2014) and from IASI in the troposphere  
373 (Wespes et al., 2017). The smaller amplitude of  $\text{O}_3$  response to QBO10 in the LSt  
374 compared to the MUST is again in agreement with previous studies that reported changes  
375 in phase of the QBO10 response as a function of altitude with a positive response in the  
376 upper stratosphere and destructive interference in the mid-low stratosphere (Chipperfield  
377 et al., 1994; Brunner et al., 2006).
- 378
- 379 2. SF - In the MUST layer, the solar cycle  $\text{O}_3$  response is one of the strongest contributors  
380 and explains globally between  $\sim 2$  and 15 DU of in-phase  $\text{O}_3$  variations (i.e. higher  $\text{O}_3$   
381 values during maximum solar irradiance) with the largest amplitude over the highest  
382 latitude regions (see Fig. 5; relative contribution up to  $\sim 20\%$ ). The solar influence in LSt  
383 is more complex with regions of in-phase and out-of-phase  $\text{O}_3$  variations. The impact of  
384 solar variability on stratospheric  $\text{O}_3$  abundance is due to a combination of processes: a  
385 modification in the  $\text{O}_3$  production rates in the upper stratosphere induced by changes in  
386 spectral solar irradiance (e.g. Brasseur et al., 1993), the transport of solar proton event-  
387 produced  $\text{NO}_y$  from the mesosphere down to the mid-low stratosphere where it decreases  
388 active chlorine and bromine and, hence,  $\text{O}_3$  destruction (e.g. Jackman et al., 2000; Hood  
389 and Soukharev, 2006; and references therein) while it enhances the  $\text{O}_3$  destruction in the  
390 MUST through  $\text{NO}_x$  catalysed cycles, and its impact on the lower stratospheric dynamics  
391 including the QBO (e.g. Hood et al., 1997; Zerefos et al., 1997; Kodera and Kuroda,  
392 2002; Hood and Soukharev, 2003, Soukharev and Hood, 2006). As for the QBO, the



393 strong SF dependence at polar latitudes in the LSt with zonal asymmetry in the O<sub>3</sub>  
394 response reflects the influence of the polar vortex strength and of stratospheric warmings,  
395 and are in good agreement with previous results (e.g. Hood et al., 1997; Zerefos et al.,  
396 1997; Labitzke and van Loon, 1999; Steinbrecht et al., 2003; Coldewey-Egbers et al.,  
397 2014). It is also worth noting that because only one solar cycle is covered, the QBO and  
398 SF effects could not be completely separated because ~~of their~~ ~~they have a~~ strong  
399 interaction (e.g. McCormack et al., 2007; Roscoe et al., 2007; Kuttippurath et al., 2013).

- 400
- 401 3. EPF - The vertical component of the planetary wave Eliassen-Palm flux entering the  
402 lower stratosphere corresponds to the divergence of the wave momentum that drives the  
403 meridional residual Brewer-Dobson circulation. In agreement with previous studies (e.g.  
404 Fusco and Salby, 1999; Randel et al., 2002; Brunner et al., 2006; Weber et al., 2011),  
405 fluctuations in the BDC are shown to cause changes on stratospheric O<sub>3</sub> distribution  
406 observed from IASI: EPF largely positively contributes to the LSt O<sub>3</sub> variations at high  
407 latitudes of both hemispheres where O<sub>3</sub> is accumulated because of its long chemical  
408 lifetime, with amplitude ranging between ~20 and 100 DU (see Fig. 5 and 6; i.e. relative  
409 contribution of ~35-150%). The influence of the EPF decreases at lower latitudes where a  
410 stronger circulation induces more O<sub>3</sub> transported from the tropics to middle-high latitudes  
411 and, hence, a decrease in O<sub>3</sub> levels particularly below 20 km (Brunner et al., 2006). The  
412 influence of EP fluxes in the Arctic is the smallest in summer (see Fig.7; <~35 DU vs ~70  
413 DU in fall; the two other seasons are not shown) due to the later O<sub>3</sub> build-up in polar  
414 vortices. In the S.H., because of the formation of the O<sub>3</sub> hole, the EP influence is smaller  
415 than in the N.H. and the seasonal variations are less marked. In the MUST, the O<sub>3</sub>  
416 response attributed to variations in EPF is positive in both hemispheres, with a much  
417 lower amplitude than in the LSt (up to ~20-35 DU). The region of out-of-phase relation  
418 with negative EPF coefficients over the high southern latitudes (Fig. 5b) is likely  
419 attributable to the influence of VPSC that has correlations with EPF by construction (see  
420 Section 2.2). Furthermore, given the annual oscillations in EPF, compensation by the 1-yr  
421 harmonic term (eq. 1, Section 2) is found, but it remains weaker than the EPF  
422 contribution (data not shown), in particular at high latitudes where the EPF contribution  
423 is the largest.
- 424
- 425 4. VPSC - Identically to EPF, VPSC is shown to mainly contribute to O<sub>3</sub> variations in LSt  
426 over the polar regions (~55 DU or 40% in the N.H. vs ~60 DU or 85% in the S.H. on a  
427 longitudinal average; see Fig. 6b) but with an opposite phase (Fig. 5 and 6a). The  
428 amplitude of the O<sub>3</sub> response to VPSC reaches its maximum over the southern latitudes  
429 during the spring (~60 DU; see Fig.7a for the austral spring period), which is consistent  
430 with the role of PSCs on the polar O<sub>3</sub> depletion when there is sufficient sunlight. The  
431 strong VPSC influence found at high northern latitudes in fall (Fig. 7a) are due to  
432 compensation effects with EPF as pointed out above and verified from sensitivity tests

433 (not shown). Note also that the VPSC contribution into MUST reflects the larger  
434 correlation between the two stratospheric layers over the southern polar region (Section  
435 2.1, Fig. 1d).

436  
437 5. AERO - Five important volcanic eruptions with stratospheric impact occurred during the  
438 IASI mission (Kasatochi in 2008, Sarychev in 2009, Nabro in 2011, Sinabung in 2014  
439 and Calbuco in 2015; see Fig.3). The two major eruptions of the last decades, El Chichon  
440 (1982) and Mt. Pinatubo (1991), ~~which have~~ injected sulfur gases into the stratosphere.  
441 They have been shown to enhance PSCs particle abundances (~15-25 km altitude), to  
442 remove NO<sub>x</sub> (through reaction with the surface of the sulfuric aerosol to form nitric acid)  
443 and, hence, to make the ozone layer more sensitive to active chlorine (e.g. Hofmann et  
444 al., 1989; Hofmann et al., 1993; Portmann et al., 1996; Solomon et al., 2016). Besides  
445 this chemical effect, the volcanic aerosols also warm the stratosphere at lower latitudes  
446 through scattering and absorption of solar radiation, which further induces indirect  
447 dynamical effects (Dhomse et al., 2015; Revell et al., 2017). Even though the recent  
448 eruptions have been of smaller magnitude than El Chichon and Mt. Pinatubo, they  
449 produced sulphur ejection through the tropopause into the stratosphere (see Section 2.2,  
450 Fig.2 and Fig.3), as seen with AOD reaching  $5 \times 10^{-4}$  over the stratosphere (150-2 hPa),  
451 especially following the eruptions of Nabro (13.3°N, 41.6°E), Sinabung (3.1°N, 98.3°E)  
452 and Calbuco (41.3°S, 72.6°W). In the LSt, the regression supports an enhanced O<sub>3</sub>  
453 depletion over the Antarctic in presence of sulfur gases with a significantly negative  
454 annual O<sub>3</sub> response reaching ~25 DU (i.e. relative contribution of ~20% into O<sub>3</sub> variation;  
455 see Fig. 5b). On the contrary, enhanced O<sub>3</sub> levels in response to sulfuric acid are found in  
456 the MUST with a maximum impact of up to 10 DU (i.e. relative contribution of ~20% into  
457 the O<sub>3</sub> variation; see Fig. 5a) over the Antarctic. The change in phase in the O<sub>3</sub> response  
458 to AERO between the LSt (~15-25 km) and the MUST (~25-40 km) over the Antarctic, as  
459 well as between polar and lower latitudes in the LSt (see Fig.5 and 6a), agree well with  
460 the heterogeneous reactions on sulfuric aerosol surface, which reduce the concentration  
461 of NO<sub>x</sub> to form nitric acid, leading to enhanced O<sub>3</sub> levels above 25 km but leading to  
462 decreased O<sub>3</sub> levels due to chlorine activation below 25 km (e.g. Solomon et al., 1996).  
463 On a seasonal basis, the depletion due to the presence of sulfur gases reaches ~30 DU on  
464 a longitudinal average, over the S.H. polar region during the austral spring (see Fig.7a)  
465 highlighting the link between volcanic gases converted to sulfate aerosols and  
466 heterogeneous polar halogen chemistry.

467  
468 6. NAO – The NAO is an important mode of global climate variability, particularly in  
469 northern winter. It describes large-scale anomalies in sea level pressure systems between  
470 the sub-tropical Atlantic (Azores; high pressure system) and sub-polar (Iceland; low  
471 pressure system) regions (Hurrell, 1995). It disturbs the location and intensity of the  
472 North Atlantic jet stream that separates these two regions depending on the phase of

473 NAO. The positive (negative) phase of the NAO corresponds to larger (weaker) pressure  
474 difference between the two regions leading to stronger westerlies (easterlies) across the  
475 mid-latitudes (Barnston and Livezey, 1987). The two pressure system regions are clearly  
476 identified in the stratospheric O<sub>3</sub> response to NAO, particularly in the LSt, with positive  
477 regression coefficients above the Labrador-Greenland region and negative coefficients  
478 above the Euro-Atlantic region (Fig. 5b). Above these two sectors, the positive phase  
479 induces, respectively, an increase and a decrease in LSt O<sub>3</sub> levels. The negative phase is  
480 characterized by the opposite behaviour. That NAO pattern is in line with previous  
481 studies (Rieder et al., 2013) and was also observed from IASI in tropospheric O<sub>3</sub> (Wespes  
482 et al., 2017). The magnitude of annual LSt O<sub>3</sub> changes attributed to NAO variations  
483 reaches ~20 DU over the in-phase Labrador region (i.e. contribution of 25% relative to  
484 the O<sub>3</sub> variations), while a much lower contribution is found for the MUST (~4 DU or  
485 ~10%). The NAO coefficient in the LSt also shows that the influence of the NAO  
486 extends further into northern Asia in the case of prolonged NAO phases. The NAO has  
487 also been shown to influence the propagation of waves into the stratosphere, hence, the  
488 BDC and the strength of the polar vortex in the N.H. mid-winter (Thompson and  
489 Wallace, 2000; Schnadt and Dameris, 2003; Rind et al., 2005). That connection between  
490 the NAO and the BDC might explain the negative anomaly in the O<sub>3</sub> response to EPF in  
491 the LSt over northern Asia ~~which~~that matches the region of negative response to the  
492 NAO.

- 493
- 494 7. AAO - The extra-tropical circulation of the S.H. is driven by the Antarctic oscillation that  
495 is characterized by geopotential height anomalies south of 20°S, with high anomalies of  
496 one sign centered in the polar region and weaker anomalies of the opposing sign north of  
497 55°S (Thompson and Wallace, 2000). This corresponds well to the two band-like regions  
498 of opposite signs found for the regression coefficients of adjusted AAO in the LSt  
499 (negative coefficients centered in Antarctica and positive coefficient north of ~40°S; see  
500 Fig.5b). Similarly to the NAO, the strength of the residual mean circulation and of the  
501 polar vortex in the S.H. are modulated by the AAO through the atmospheric wave  
502 activity (Thompson and Wallace, 2000; Thompson and Solomon, 2001). During the  
503 positive (negative) phase of the AAO, the BDC is weaker (stronger) leading to less  
504 (more) O<sub>3</sub> transported from the tropics into the southern polar region, and the polar  
505 vortex is stronger (weaker) leading to more (less) O<sub>3</sub> depletion inside. This likely  
506 explains both the positive AAO coefficients in the region north of ~40°S (contribution <  
507 ~5 DU or ~10%) and the negative coefficients around and over the Antarctic  
508 (contribution reaching ~10 DU or ~15%; exception is found with positive coefficients  
509 over the western Antarctic). The dependence of O<sub>3</sub> variations to the AAO in the MUST is  
510 lower than ~7 DU (or ~15%).

511

512 8. ENSO - Besides the NAO and the AAO, the El Niño southern oscillation is another  
513 dominant mode of global climate variability. This coupled ocean-atmosphere  
514 phenomenon is governed by sea surface temperature (SST) differences between high  
515 tropical and low extra-tropical Pacific regions (Harrison and Larkin, 1998). Domeisen et  
516 al. (2019) have recently reviewed the possible mechanisms connecting the ENSO to the  
517 stratosphere in the tropics and the extratropics of both hemispheres. The ozone response  
518 to ENSO is represented in Fig. 5 only for the ENSO-lag3 proxy which is found to be the  
519 main ENSO proxy contributing to the observed O<sub>3</sub> variations. While in the troposphere,  
520 previous works have shown that the ENSO influence mainly results in a high contrast of  
521 the regression coefficients between western Pacific/Indonesia/North Australia and  
522 central/eastern Pacific regions caused by reduced rainfalls and enhanced O<sub>3</sub> precursor  
523 emissions above western Pacific (called “chemical effect”) (e.g. Oman et al., 2013;  
524 Valks et al., 2014; Ziemke et al., 2015; Wespes et al., 2016; and references therein), the  
525 LSt O<sub>3</sub> response to ENSO is shown here to translate into a strong tropical-extratropical  
526 gradient in the regression coefficients with a negative response in the tropics and a  
527 positive response at higher latitudes (~5 DU and ~10 DU, respectively, on longitudinal  
528 averages; see Fig. 6a). In the MSt, ENSO is globally a smaller out-of-phase driver of O<sub>3</sub>  
529 variations (response of ~5 DU). The decrease in LSt O<sub>3</sub> during the warm ENSO phase in  
530 the tropics (characterized by a negative ENSO lag-3 coefficient reaching 7 DU (or 35%),  
531 respectively, in the LSt; see Fig. 5) is consistent with the ENSO-modulated upwelling via  
532 deep convection in the tropical lower stratosphere and, hence, increased BD circulation  
533 (e.g. Randel et al., 2009). The in-phase accumulation of LSt O<sub>3</sub> in the extra-tropics  
534 (contribution reaching 15 DU or 20%; see Fig. 5) is also consistent with enhanced extra-  
535 tropical planetary waves that propagate into the stratosphere during the warm ENSO  
536 phase, resulting in sudden stratospheric warmings and, hence, in enhanced BDC and  
537 weaker polar vortices (e.g. Brönnimann et al., 2004; Manzini et al., 2006; Cagnazzo et  
538 al., 2009). The very pronounced link between stratospheric O<sub>3</sub> and the ENSO related  
539 dynamical pathways with a time lag of about 3 months is one key finding of the present  
540 work. Indeed, the influence of ENSO on stratospheric O<sub>3</sub> measurements has already been  
541 reported in earlier studies (Randel and Cobb, 1994; Brönnimann et al., 2004; Randel et  
542 al., 2009; Randel and Thompson, 2011; Oman et al., 2013; Manatsa and Mukwada, 2017;  
543 Tweedy et al., 2018), but it is the first time that a delayed stratospheric O<sub>3</sub> response is  
544 investigated in MLR studies. A 4- to 6-month time lag in O<sub>3</sub> response to ENSO has  
545 similarly been identified from IASI in the troposphere (Wespes et al., 2017), where it was  
546 explained not only by a tropospheric pathway but also by a specific stratospheric pathway  
547 similar to that modulating stratospheric O<sub>3</sub> but with further impact downward onto  
548 tropospheric circulation (Butler et al., 2014; Domeisen et al., 2019). Furthermore, the 3-  
549 month lag identified in the LSt O<sub>3</sub> response is fully consistent with the modelling work of  
550 Cagnazzo et al. (2009) that reports a warming of the polar vortex in February-March  
551 following a strong ENSO event (peak activity in November-December) associated with

552 positive O<sub>3</sub> ENSO anomaly reaching ~10 DU in the Arctic and negative anomaly of ~6-7  
553 DU in the Tropics. We find that the tropical-extra-tropical gradient in O<sub>3</sub> response to  
554 ENSO-lag3 is indeed much stronger in spring with contributions of ~20-30 DU (see  
555 Fig.7a for the austral spring period vs winter).

556  
557 Overall, although the annual MLR model underestimates the O<sub>3</sub> variability at high latitudes  
558 (>50°N/S) by up to 5 DU, particularly in the MUST (see Fig. 6b), we conclude that it gives a  
559 good overall representation of the sources of O<sub>3</sub> variability in the two stratospheric layers  
560 sounded by IASI. This is particularly true for the spring period (see Fig. 7) which was studied in  
561 several earlier works to reveal the onset of Antarctic total O<sub>3</sub> recovery (Salby et al., 2011;  
562 Kuttippurath et al., 2013; Shepherd et al., 2014; Solomon et al., 2016; Weber et al., 2018),  
563 despite the large O<sub>3</sub> variability due to the hole formation during that period (~80 DU; see Fig.7a,  
564 LSt panel). It is also interesting to see from Fig.7 that the broad O<sub>3</sub> depletion over Antarctica in  
565 the LSt is attributed by the MLR to VPSC (up to 60 DU of explained O<sub>3</sub> variability on a  
566 latitudinal average). Following these promising results, we further analyze below the O<sub>3</sub>  
567 variability in response to anthropogenic perturbations, assumed in the MLR model by the linear  
568 trend term, with a focus over the polar regions.

## 569 **4 Trend analysis**

### 570 **4.1 10-year trend detection in stratospheric layers**

571  
572 The distributions of the linear trend estimated by the annual regression are represented in Fig. 8a  
573 for the MUST and the LSt (left and right panels). In agreement with the early signs of O<sub>3</sub>  
574 recovery reported for the extra-tropical mid- and upper stratosphere above ~25-10 hPa (>25-30  
575 km; Pawson et al., 2014; Harris et al., 2015; Steinbrecht et al., 2017; Sofieva et al., 2017; Ball et  
576 al., 2018), the MUST shows significant positive trends larger than 1 DU/yr poleward of ~35°N/S  
577 (except over Antarctica). The corresponding decadal trends (>10 DU/decade) are much larger  
578 than the discontinuity of ~2-4 DU encountered in the MUST record on 15 September 2010 and  
579 discussed in section 2.1. The tropical MUST also shows positive trends but they are weaker (<0.8  
580 DU/yr) or not significant. The largest increase is observed in polar O<sub>3</sub> with amplitudes reaching  
581 ~2.0 DU/yr. The mid-latitudes also show significant O<sub>3</sub> enhancement which can be attributed to  
582 air mass mixing after the disruption of the polar vortex (Knudsen and Grooss, 2000; Fioletov and  
583 Shepherd, 2005; Dhomse, 2006; Nair et al., 2015).

584  
585  
586  
587 As in the MUST, the LSt is characterized in the southern polar latitudes by significantly positive  
588 and large trends (between ~ 1.0 and 2.5 DU/yr). In the mid-latitudes, the lower stratospheric  
589 trends are significantly negative, i.e. opposite to those obtained in the MUST. This highlights the  
590 independence between the two O<sub>3</sub> layers sounded by IASI in the stratosphere. Poleward of 25°N  
591 the negative LSt trends range between ~ -0.5 and -1.7 DU/yr. Negative trends in lower

592 stratospheric O<sub>3</sub> have already been reported in extra-polar regions from other space-based  
593 measurements (Kyrölä et al., 2013; Gebhardt et al., 2014; Sioris et al., 2014; Harris et al., 2015;  
594 Nair et al., 2015; Vigouroux et al., 2015; Wespes et al., 2016; Steinbrecht et al., 2017; Ball et al.,  
595 2018) and may be due to changes in stratospheric dynamics at the decadal timescale (Galytska et  
596 al., 2019). These previous studies, which were characterized by large uncertainties or resulted  
597 from composite-data merging techniques, are confirmed here using a single dataset. The negative  
598 trends which are observed at lower stratospheric middle latitudes are difficult to explain with  
599 chemistry-climate models (Ball et al., 2018). It is also worth noting that the significant MUST and  
600 LSt O<sub>3</sub> trends are of the same order as those previously estimated from IASI over a shorter  
601 period (from 2008 to 2013) and latitudinal averages (see Wespes et al., 2016). This suggests that  
602 the trends are not very sensitive to the natural variability in the IASI time series, hence,  
603 supporting the significance of the O<sub>3</sub> trends presented here.

604

605 The sensitivity of IASI O<sub>3</sub> to the estimated trend from MLR is further verified in Fig. 8b that  
606 represents the global distributions of relative differences in the *RMSE* of the regression residuals  
607 obtained with and without a linear trend term included in the MLR model ( $(RMSE_{w/o\_LT} -$   
608  $RMSE_{with\_LT})/RMSE_{with\_LT} \times 100$ ; in %). An increase of ~1.0-4.0% and ~0.5-2.0% in the *RMSE*  
609 is indeed observed for both the MUST and the LSt, respectively, in regions of significant trend  
610 contribution (Fig. 8a), when the trend is excluded. This demonstrates the significance of the  
611 trend in improving the performance of the regression. Another statistical method that can be used  
612 for evaluating the possibility to infer, from the IASI time period, the significant positive or  
613 negative trends in the MUST and the LSt, respectively, consists in determining the expected year  
614 when these specified trends would be detectable from the available measurements (with a  
615 probability of 90%) by taking into account the variance ( $\sigma_\epsilon^2$ ) and the autocorrelation ( $\Phi$ ) of the  
616 noise residual according to the formalism of Tiao et al. (1990) and Weatherhead et al. (1998).  
617 The 95% confidence interval for that expected trend detection year can also be determined. Such  
618 a method has already been used for evaluating the trends derived from IASI in the troposphere  
619 (Wespes et al., 2018). It represents a more drastic and conservative method than the standard  
620 MLR. The results are displayed in Fig. 8c for an assumed specified trend of |1.5| DU/yr, which  
621 corresponds to a medium amplitude of trends derived here above from the MLR over the mid-  
622 polar regions (Fig. 8a). In the MUST, we find that ~2-3 additional years of IASI measurements  
623 would be required to unequivocally detect a trend of |1.5| DU/yr (with probability 0.90) over  
624 high latitudes (detectable from ~2020-2022  $\pm$  6-12 months) whereas it should already be  
625 detectable over the mid- and lower latitudes (from ~2015  $\pm$  3-6 months). In the LSt, an additional  
626 ~7 years ( $\pm$  1-2 years) of IASI measurements would be required to categorically identify the  
627 probable decline derived from the MLR in northern mid-latitudes, and even more to measure the  
628 enhancement in the southern polar latitudes. The longer required measurement period at high  
629 latitudes is due to the larger noise residuals in the regression fits (i.e. largest  $\sigma_\epsilon$ ) at these  
630 latitudes (see Fig.4 a and b). Note that a larger specified trend amplitude would obviously require



631 a shorter period of IASI measurement. We find that only ~2 additional years would be required  
632 to detect a specified trend of  $|2.5|$  DU/yr which characterizes the LSt at high latitudes (data not  
633 shown).

#### 634 **4.2 Stratospheric contributions to total O<sub>3</sub> trend**

635  
636  
637 The effect on total O<sub>3</sub> of the counteracting trends in the northern mid-latitudes and of the  
638 constructive trends in the southern polar latitudes in the two stratospheric layers sounded by IASI  
639 is now investigated.

640  
641 Figure 9 represents the global distributions of the contribution of the MUST and the LSt into the  
642 total O<sub>3</sub> columns (Fig.9a; in %), of the adjusted trends for the total O<sub>3</sub> (Fig. 9b in DU/yr) and of  
643 the estimated year for a  $|1.5|$  DU/yr trend detection with a probability of 90% (Fig. 9c). While no  
644 significant change or slightly positive trends in total O<sub>3</sub> after the inflection point in 1997 have  
645 been reported on an annual basis (e.g; Weber et al., 2018), Fig. 9b shows clear significant  
646 changes: negative trend at northern mid- and high latitudes (up to ~2.0 DU/yr north of 30°N) and  
647 positive trend over the southern polar region (up to ~3.0 DU/yr south of 45°S). Although  
648 counteracting trends between lower and upper stratospheric O<sub>3</sub> have been pointed out in the  
649 recent study of Ball et al. (2018) to explain the non-significant recovery in total O<sub>3</sub>, we find from  
650 IASI a dominance of the LSt decline that translates to negative trends over some regions of the  
651 N.H. mid- and high latitudes in TOC (Fig. 9b). This is explained by the contributions of 45-55%  
652 from the LSt to the total column, vs ~30-40% from the MUST (Fig. 9a) in the mid- and polar  
653 regions over the whole year. In addition, the increase in total O<sub>3</sub> at high southern latitudes is  
654 dominated by the LSt, although both layers positively contribute around Antarctica, comparing  
655 to the trend distributions in Fig. 8. Note that most previous ozone trends studies, including Ball  
656 et al. (2018), excluded the polar regions due to limited latitude coverage of some instruments  
657 merged in the data composites.

658  
659 While the annual MLR shows a significant dominance of LSt trends over MUST trends in the  
660 northern mid-latitudes and significant constructive trends in the southern latitudes, total O<sub>3</sub>  
661 trends are not ascribed with complete confidence according to the formalism of Tiao et al. (1990)  
662 and Weatherhead et al. (1998) discussed in Section 4.1. The detectability of a specified trend of  
663  $|1.5|$  DU/yr (Fig. 9c), which corresponds to the medium trend derived from MLR in mid-high  
664 latitudes of both hemispheres (Fig. 9b), would need several years of additional measurements to  
665 be unequivocal from IASI on an annual basis (from ~2022–2024 over the mid-latitudes and  
666 from ~2035 over the polar regions). A higher trend amplitude of  $\sim|2.5|$  DU/yr derived from the  
667 MLR would be observable from ~2020-2025 (figure not shown).

668

669 The use of the annual MLR could translate to large systematic uncertainties on trends (implying  
670 large  $\sigma_\epsilon$ ), which induces a longer measurement period required to yield significant trends. These  
671 uncertainties could be reduced on a seasonal basis, by attributing different weights to the  
672 seasons, which would help in the categorical detection of a specified trend. This is investigated  
673 in the subsection below by focusing on the winter and the spring periods.

674

### 675 **4.3 Trends in spring and winter**

676

677 The reports on early signs of total O<sub>3</sub> recovery (Salby et al., 2011; Kuttippurath et al., 2013;  
678 Shepherd et al., 2014; Solomon et al., 2016; Kuttippurath and Nair, 2017; Weber et al., 2018)  
679 have all focused on the Antarctic region during spring/summer, when the ozone hole area is at its  
680 maximum extent, i.e. the LSt O<sub>3</sub> levels at minimum values. [Kuttippurath et al. \(2018\) also](#)  
681 [reported a significant reduction in Antarctic O<sub>3</sub> loss saturation occurrences during spring.](#) Here  
682 we investigate the respective contributions of the LSt and the MUST to the TOC recovery over  
683 the Southern latitudes during spring and also during winter when the minima in O<sub>3</sub> levels occur  
684 in the MUST (down to ~60 DU in polar regions), in comparison with the Northern latitudes.  
685 Figures 10 and 11, respectively, show the S.H. and the N.H. distributions of the estimated trends  
686 from seasonal MLR (left panels) and of the corresponding year required for a significant  
687 detection of |3.0| DU increase per year (right panels) during their respective winter (JJA and DJF;  
688 Fig. 10a and 11a) and spring (SON and MAM; Fig. 10b and 11b) for the total, MUST and LSt O<sub>3</sub>  
689 (top, middle and bottom panels, respectively). Fig. 10 a and b clearly show significant positive  
690 trends over Antarctica and the southernmost latitudes of the Atlantic and Indian oceans, with  
691 amplitudes ranging between ~1-5 DU/yr over latitudes south of ~35-40°S in total, MUST and LSt  
692 O<sub>3</sub> (~3.6±2.7 DU/yr, ~3.0±1.3 DU/yr, ~3.6±3.1 DU/yr and ~3.7±1.7 DU/yr, ~1.3±0.7 DU/yr,  
693 ~3.7±1.6 DU/yr, on spatial averages, respectively over JJA and SON, for the three O<sub>3</sub> columns).  
694 These trends over 10 years are much larger than the amplitude of the discontinuity in the MUST  
695 time series (section 2.1) and than the trends estimated in Sections 4.1 (see Fig.8 for the MUST  
696 and the LSt) and 4.2 (see Fig.9 for TOC) over the whole year. In MUST, significant positive  
697 trends are observed during each season over the mid- and polar latitudes of both hemispheres  
698 (Fig. 10 and 11 for the winter and spring periods; the other seasons are not shown here) but more  
699 particularly in winter and in spring where the increase reaches a maximum of ~4 DU/yr. In the  
700 LSt, the distributions are more complex: the trends are significantly negative in the mid-latitudes  
701 of both hemispheres, especially in winter and in spring of the N.H., while in spring of the S.H.,  
702 some mid-latitude regions also show near-zero or even positive trends. The southern polar region  
703 shows high significant positive trends in winter/spring (see Fig.10). For the total O<sub>3</sub> at mid-high  
704 latitudes, given the mostly counteracting trends detected in the LSt and in the MUST and the  
705 dominance of the LSt over the MUST (~45-55% from the LSt vs ~30-40% from the MUST into  
706 total O<sub>3</sub> over the whole year;), these latitudes are governed by negative trends, especially in  
707 spring of the N.H. High significant increases are detected over polar regions in winter/spring of

708 both hemispheres but more particularly in the S.H. where the LSt and MUST trends are both of  
709 positive sign.

710  
711 The substantial winter/spring positive trends observed in MUST, LSt and total O<sub>3</sub> levels at high  
712 latitudes of the S.H. (and of the N.H. for the MUST) are furthermore demonstrated to be  
713 detectable from the available IASI measurement period (see Fig. 10, right panels: an assumed  
714 increase of |3.0| DU/yr is detectable from 2016 ± 6 months and from 2018 ± 1 year in the MUST  
715 and the LSt, respectively). The positive trend of ~4 DU/yr measured in polar total O<sub>3</sub> in  
716 winter/spring would be observable from ~2018-2020 ± 1-2 year and the decline of ~-3 DU/yr in  
717 winter/spring of the N.H. in LSt would be detectable from ~2018-2020 ± 9 months (not shown  
718 here). Note that the higher negative trends found above the Pacific at highest latitudes (see Fig.  
719 10) correspond to the regions with longest required measurement period for significant trend  
720 detection and, hence, point to poor regression residuals. About ~50% and ~35% of the  
721 springtime MUST and LSt O<sub>3</sub> variations, respectively, are due to anthropogenic factors (estimated  
722 by VPSC×EESC proxy and linear trend in MLR models). This suggests that O<sub>3</sub> changes  
723 especially in the LSt are mainly governed by dynamics, which contributes to a later projected  
724 trend-detection year in comparison with the MUST (Fig. 10 and 11) and which may hinder the O<sub>3</sub>  
725 recovery process.

726  
727 Overall, the large positive trends estimated concurrently in LSt, MUST and total O<sub>3</sub> over the  
728 Antarctic region in winter/spring likely reflect the healing of the ozone layer with a decrease of  
729 polar ozone depletion (Solomon et al., 2016) and, hence, demonstrate the efficiency of the  
730 Montreal protocol. To the best of our knowledge, these results represent the first detection of a  
731 significant recovery in the stratospheric and the total O<sub>3</sub> columns over the Antarctic from one  
732 single satellite dataset.

733

#### 734 **4.4 Speeding up in O<sub>3</sub> changes**

735

736 Positive trends in total O<sub>3</sub> have already been determined earlier by Solomon et al. (2016) and by  
737 Weber et al. (2018) over Antarctica during September over earlier periods (~2.5±1.5DU/yr over  
738 2000-2014 and 8.2±6.2%/dec over 2000-2016, respectively). The larger trends derived from the  
739 IASI records (see Fig.10b; ~3.7±1.7 DU/yr or ~14.4±5.8%/dec on average in TOC during SON)  
740 suggest that the O<sub>3</sub> response could be speeding up due to the accelerating decline of O<sub>3</sub> depleting  
741 substances (ODS) resulting from the Montreal Protocol. This has been investigated here by  
742 estimating the change in trend in MUST, LSt and total O<sub>3</sub> over the IASI mission. Knowing that  
743 the length of the measurement period is an important criterion for reducing systematic errors in  
744 the trend coefficient determination (i.e. the specific length of natural mode cycles should be  
745 covered to avoid any possible compensation effect between the covariates), the ozone response  
746 to each natural driver (including VPSC) taken from their adjustment over the whole IASI period  
747 (2008-2017; Section 3, Fig.5) is kept fixed. The linear trend term only is adjusted over variable

748 measurement periods that all end in December 2017, by using a single linear iteratively  
749 reweighted least squares regression applied on gridded daily IASI time series, after all the  
750 sources of natural variability fitted over the full IASI period are removed (typical examples of  
751 linear trend adjustment can be found in ~~the~~ Fig. S2 of the supplementary materials). The  
752 discontinuity found in the MUsT IASI O<sub>3</sub> records on September 2010 (see Section 2.1) is not  
753 taken into account in the regression; hence, it might over-represent the trends estimated over  
754 periods that start before the jump (i.e. 2008-2017, 2009-2017, 2010-2017). The zonally averaged  
755 results are displayed in Fig. 12 for the statistically significant total, MUsT and LSt O<sub>3</sub> trends and  
756 their associated uncertainty (accounting for the autocorrelation in the noise residuals; in the 95%  
757 confidence level) estimated from an annual regression. Note that the results are only shown for  
758 periods starting before 2015 as too short periods induce too large standard errors. In the LSt, a  
759 clear speeding up in the southern polar O<sub>3</sub> recovery is observed with amplitude ranging from  
760  $\sim 1.5 \pm 0.4$  DU/yr over 2008-2017 to  $\sim 5.5 \pm 2.5$  DU/yr over 2015-2017 on zonal averages.  
761 Similarly, a speeding of the O<sub>3</sub> decline at northern mid-latitudes is found with values ranging  
762 between  $\sim -0.7 \pm 0.2$  DU/yr over 2008-2017 and  $\sim -2.8 \pm 1.2$  DU/yr over 2015-2017. In the MUsT, a  
763 weaker increase is observed over the year around  $\sim 60^\circ$  latitude of the S.H. (from  $\sim 0.8 \pm 0.2$  DU/yr  
764 over 2008-2017 to  $\sim 2.5 \pm 1.3$  DU/yr over 2015-2017). Given the positive acceleration in both LSt  
765 and MUsT O<sub>3</sub> in the S.H., this is where the total O<sub>3</sub> record is characterized by the largest  
766 significant recovery (from  $\sim 1.7 \pm 0.7$  DU/yr over 2008-2017 to  $\sim 8.0 \pm 3.5$  DU/yr over 2015-2017).  
767 Surprisingly, the speeding up in the O<sub>3</sub> decline in the N.H. is more pronounced in the total O<sub>3</sub>  
768 (from  $\sim -1.0 \pm 0.4$  DU/yr over 2008-2017 to  $\sim -5.0 \pm 2.5$  DU/yr over 2015-2017) compared to the  
769 LSt, despite the opposite trend in MUsT O<sub>3</sub>. This could reflect the O<sub>3</sub> decline observed in the  
770 northern latitudes in the troposphere ( $\sim -0.5$  DU/yr over 2008-2016; cfr Wespes et al., 2018)  
771 which is included in the total column.

772  
773 Overall, the larger annual significant trend amplitudes derived over the last few years of total,  
774 MUsT and LSt O<sub>3</sub> measurements, compared with those derived from the whole studied period  
775 (Sections 4.1 and 4.2) and from earlier studies, translate to trends that remain detectable over the  
776 increasing uncertainty associated ~~to~~with the shorter and shorter time segments (see Fig. S3 of the  
777 supplementary materials), especially in both LSt and total O<sub>3</sub> in the S.H. This demonstrates that  
778 we progress towards a significant emergence and speeding up of O<sub>3</sub> recovery process in the  
779 stratosphere over the whole year. Nevertheless, we calculated that additional years of IASI  
780 measurements would help in confirming the changes in O<sub>3</sub> recovery and decline over the IASI  
781 period (e.g.  $\sim 4$  additional years are required to verify the trends calculated over the 2015-2017  
782 segment in the highest latitudes in LSt). In addition, a longer measurement period would be  
783 useful to derive trends over successive segments of same length that are long enough to reduce  
784 the uncertainty, in order to make the trend and its associated uncertainty more comparable across  
785 the fit.

## 786 787 **5 Summary and conclusion**

788

789 In this study, we have analysed the changes in stratospheric O<sub>3</sub> levels sounded by IASI-A by  
790 examining the global pictures of natural and anthropogenic sources of O<sub>3</sub> changes independently  
791 in the lower (150-25 hPa) and in the mid-upper stratosphere (<25 hPa). We have exploited to that  
792 end a multi-linear regression model that has been specifically developed for the analysis of  
793 stratospheric processes by including a series of drivers known to have a causal relationship to  
794 natural stratospheric O<sub>3</sub> variations, namely SF, QBO-10, QBO-30, NAO, AAO, ENSO, AERO,  
795 EPF and VPSC. We have first verified the representativeness of the O<sub>3</sub> response to each of these  
796 natural drivers and found for most of them characteristic patterns that are in line with the current  
797 knowledge of their dynamical influence on O<sub>3</sub> variations. One of the most important finding  
798 related to the O<sub>3</sub> driver analysis relied on the detection of a very clear time lag of 3 months in the  
799 O<sub>3</sub> response to ENSO in the LSt, with a pronounced contrast between an in-phase response in the  
800 extra-tropics and an out-of-phase response in the tropics, which is consistent with the ENSO-  
801 modulated dynamic. The 3-month lag observed in the lower stratosphere is also coherent with  
802 the 4- to -6 months lag detected from a previous study in the troposphere (Wespes et al., 2017)  
803 and further supports the stratospheric pathway suggested in Butler et al. (2014) to explain an  
804 ENSO influence over a long distance. The representativeness of the influence of the O<sub>3</sub> drivers  
805 was also confirmed on a seasonal basis (e.g. high ENSO-lag3 effect in spring, strong VPSC and  
806 AERO influences during the austral spring ...). These results have verified the performance of  
807 the regression models (annual and seasonal) to properly discriminate between natural and  
808 anthropogenic drivers of O<sub>3</sub> changes. The anthropogenic influence has been evaluated with the  
809 linear trend adjustment in the MLR. The main results are summarized as follows:

810

811 (i) A highly probable (within 95%) recovery process is derived from the annual MLR at high  
812 southern latitudes in the two stratospheric layers and, therefore, in the total column. It  
813 is also derived at high northern latitudes in the MUST. However, a longer period of  
814 IASI measurements is needed– to unequivocally demonstrate a positive trend on  
815 annual basis in the IASI record. Only ~2-3 additional years of IASI measurements are  
816 required in the MUST.

817

818 (ii) A likely O<sub>3</sub> decline (within 95%) is measured in the lower stratosphere at mid-latitudes,  
819 specifically, of the N.H., but it would require an additional ~7 years of IASI  
820 measurements to be categorically confirmed. Given the large contribution from the  
821 LSt to the total column (~45-50% from LSt vs ~35% from the MUST into TOCs), the  
822 decline is also calculated in total O<sub>3</sub> with ~4-6 years of additional measurements for  
823 the trend to be unequivocal.

824

825 (iii) A significant O<sub>3</sub> recovery is categorically found in the two stratospheric layers  
826 (>~35°N/S in the MUST and >~45°S in the LSt) as well as in the total column  
827 (>~45°S) during the winter/spring period, which confirms previous studies that

828 showed healing in the Antarctic O<sub>3</sub> hole with a decrease of its areal extent. These  
829 results verify the efficacy of the ban on O<sub>3</sub> depleting substances imposed by the  
830 Montreal protocol and its amendments, throughout the stratosphere and in the total  
831 column, from only one single satellite dataset for the first time.

832  
833 (iv) The decline observed in LSt O<sub>3</sub> at northern mid-latitudes is unequivocal over the  
834 available IASI measurements in winter/spring of the N.H. The exact reasons for that  
835 decline are still unknown but O<sub>3</sub> changes in the LSt are estimated to be mainly  
836 attributable to dynamics which likely perturbs the healing of LSt and total O<sub>3</sub> in the  
837 N.H.

838  
839 (v) A significant speeding up (within 95%) in that decline is measured in LSt and total O<sub>3</sub>  
840 over the last 10 years (from  $\sim -0.7 \pm 0.2$  DU/yr over 2008-2017 to  $\sim -2.8 \pm 1.2$  DU/yr  
841 over 2015-2017 in LSt O<sub>3</sub> on zonal averages). Even if the acceleration cannot be  
842 categorically confirmed yet, it is of particular urgency to understand its causes for  
843 apprehending its possible impact on the O<sub>3</sub> layer and on future climate changes.

844  
845 (vi) A clear and significant speeding up (within 95%) in stratospheric and total O<sub>3</sub> recovery  
846 is measured at southern latitudes (e.g. from  $\sim 1.5 \pm 0.4$  DU/yr over 2008-2017 to  
847  $\sim 5.5 \pm 2.5$  DU/yr over 2015-2017 in the LSt), which translate to trend values that  
848 would be categorically detectable in the next few years on an annual basis. It  
849 demonstrates that we are currently progressing towards a substantial emergence in O<sub>3</sub>  
850 healing in the stratosphere over the whole year in the S.H..

851  
852 Additional years of IASI measurements that will be provided by the operational IASI-C (2018)  
853 on flight and the upcoming IASI-Next Generation (IASI-NG) instrument onboard the Metop  
854 Second Generation (Metop-SG) series of satellites would be of particular interest to confirm and  
855 monitor, in the near future and over a longer period, the speeding up in the O<sub>3</sub> healing of the S.H.  
856 as well as in the LSt O<sub>3</sub> decline measured at mid-latitudes of the N.H. IASI-NG/Metop-SG is  
857 expected to extend the data record much further in the future (Clerbaux and Crevoisier, 2013;  
858 Crevoisier et al., 2014).

#### 859 **Data availability**

860  
861  
862 The IASI O<sub>3</sub> data processed with FORLI-O<sub>3</sub> v0151001 can be downloaded from the Aeris portal  
863 at: <http://iasi.aeris-data.fr/O3/> (last access: 134 JulySeptember 2019).

#### 864 **Author contribution**

865  
866



867 C.W. performed the analysis, wrote the manuscript and prepared the figures. D.H. was  
868 responsible for the retrieval algorithm development and the processing of the IASI O<sub>3</sub> dataset.  
869 All co-authors contributed to the analysis and reviewed the manuscript.

870

### 871 **Competing interests**

872

873 The authors declare that they have no conflict of interest.

874

### 875 **Acknowledgments**

876

877 IASI has been developed and built under the responsibility of the Centre National d'Etudes  
878 Spatiales (CNES, France). It is flown onboard the Metop satellites as part of the EUMETSAT  
879 Polar System. The IASI L1 data are received through the EUMETCast near real time data  
880 distribution service. We acknowledge the financial support from the ESA O<sub>3</sub>-CCI and  
881 Copernicus O<sub>3</sub>-C3S projects. FORLI-O<sub>3</sub> is being implemented at Eumetsat with the support of  
882 the AC SAF project. The research in Belgium is also funded by the Belgian State Federal Office  
883 for Scientific, Technical and Cultural Affairs and the European Space Agency (ESA Prodex IASI  
884 Flow and B-AC SAF). We acknowledge Ingo Wohltmann (Alfred Wagner Institute, Postdam,  
885 Germany) as well as Beiping Luo (Institute for Atmosphere and Climate, ETH Zurich,  
886 Switzerland) and Larry Thomason (NASA Langley Research Center, Hampton, USA), for  
887 processing and providing datasets of volume of polar stratospheric clouds and of sulfuric acid  
888 extinction coefficients, respectively. We are also grateful to Maxime Prignon (Université de  
889 Liège, Liège, Belgium) for providing several years of BASCOE simulations.

890

891

892

893

894

895

896

897

898

899

900

901

902

903

904

905

906

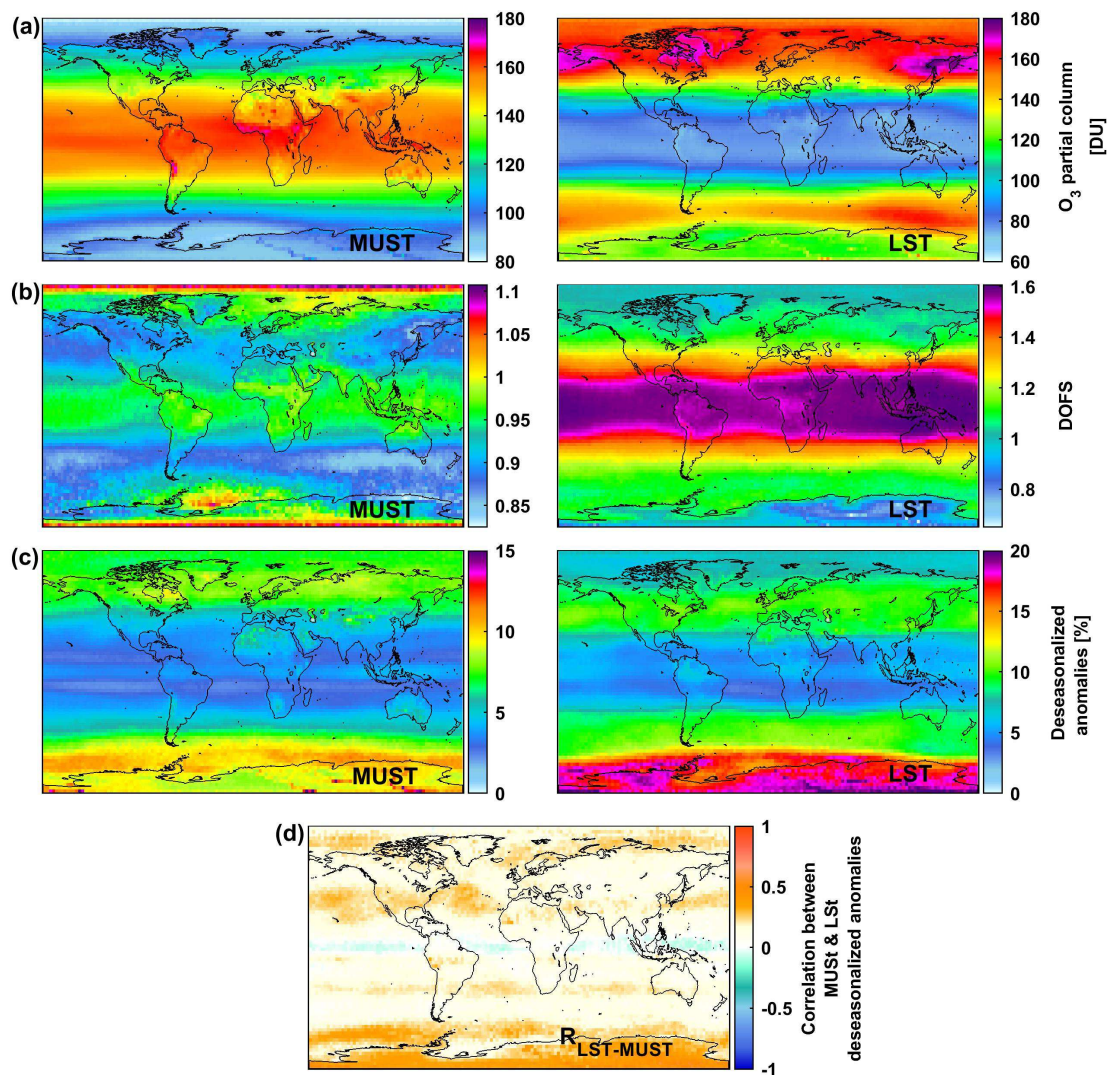
907 **Table 1** List of the explanatory variables used in the multi-linear regression model applied on  
 908 IASI stratospheric O<sub>3</sub>, their temporal resolution and their sources.  
 909

Proxy	Description ( <i>resolution</i> )	Sources
<b>F10.7</b>	The 10.7 cm solar radio flux ( <i>daily</i> )	NOAA National Weather Service Climate Prediction Center: <a href="ftp://ftp.ngdc.noaa.gov/STP/space-weather/solar-data/solar-features/solar-radio/noontime-flux/penticton/penticton_adjusted/listings/listing_drao_noontime-flux-adjusted_daily.txt">ftp://ftp.ngdc.noaa.gov/STP/space-weather/solar-data/solar-features/solar-radio/noontime-flux/penticton/penticton_adjusted/listings/listing_drao_noontime-flux-adjusted_daily.txt</a>
<b>QBO<sup>10</sup></b> <b>QBO<sup>30</sup></b>	Quasi-Biennial Oscillation index at 10hPa and 30hPa ( <i>monthly</i> )	Free University of Berlin: <a href="http://www.geo.fu-berlin.de/en/met/ag/strat/produkte/qbo/">www.geo.fu-berlin.de/en/met/ag/strat/produkte/qbo/</a>
<b>EPF</b>	Vertical component of Eliassen-Palm flux crossing 100 hPa, averaged over 45°-75° for each hemisphere and accumulated over the 3 or 12 last months depending on the time period and the latitude (see text for more details) ( <i>daily</i> )	Calculated at ULB from the NCEP/NCAR gridded reanalysis: <a href="https://www.esrl.noaa.gov/psd/data/gridded/data.ncep.reanalysis.html">https://www.esrl.noaa.gov/psd/data/gridded/data.ncep.reanalysis.html</a>
<b>AERO</b>	Stratospheric volcanic aerosols; Vertically integrated sulfuric acid extinction coefficient at 12 μm over 150-25 hPa and 25-2hPa, averaged over the tropics and the extra-tropics north and south (see text for more details) ( <i>monthly</i> )	Extinction coefficients processed at the Institute for Atmosphere and Climate (ETH Zurich, Switzerland; Thomason et al., 2018)
<b>VPSC</b>	Volume of Polar Stratospheric Clouds for the N.H. and the S.H. multiplied by the equivalent effective stratospheric chlorine (EESC) and accumulated over the 3 or 12 last months (see text for details) ( <i>daily</i> )	Processed at the Alfred Wagner Institute (AWI, Potsdam, Germany; Ingo Wolthmann, private communication)  EESC taken from the Goddard Space Flight Center: <a href="https://acd-ext.gsfc.nasa.gov/Data_services/automailer/index.html">https://acd-ext.gsfc.nasa.gov/Data_services/automailer/index.html</a>
<b>ENSO</b>	Multivariate El Niño Southern Oscillation Index (MEI) (2- <i>monthly averages</i> )	NOAA National Weather Service Climate Prediction Center: <a href="http://www.esrl.noaa.gov/psd/enso/mei/table.html">http://www.esrl.noaa.gov/psd/enso/mei/table.html</a>
<b>NAO</b>	North Atlantic Oscillation index for the N.H. ( <i>daily</i> )	<a href="ftp://ftp.cpc.ncep.noaa.gov/cwlinks/norm.daily.nao.index.b500101.curent.ascii">ftp://ftp.cpc.ncep.noaa.gov/cwlinks/norm.daily.nao.index.b500101.curent.ascii</a>
<b>AAO</b>	Antarctic Oscillation index for the S.H. ( <i>daily</i> )	<a href="ftp://ftp.cpc.ncep.noaa.gov/cwlinks/norm.daily.aao.index.b790101.curent.ascii">ftp://ftp.cpc.ncep.noaa.gov/cwlinks/norm.daily.aao.index.b790101.curent.ascii</a>
<b>GEO</b>	Geopotential height at 200 hPa (2.5°x2.5° gridded) ( <i>daily</i> )	<a href="http://apps.ecmwf.int/datasets/data/interim-full-daily/?levtype=pl">http://apps.ecmwf.int/datasets/data/interim-full-daily/?levtype=pl</a>
<b>PV</b>	Potential vorticity at 200 hPa (2.5°x2.5° gridded) ( <i>daily</i> )	

910 **Figure captions**

911

912

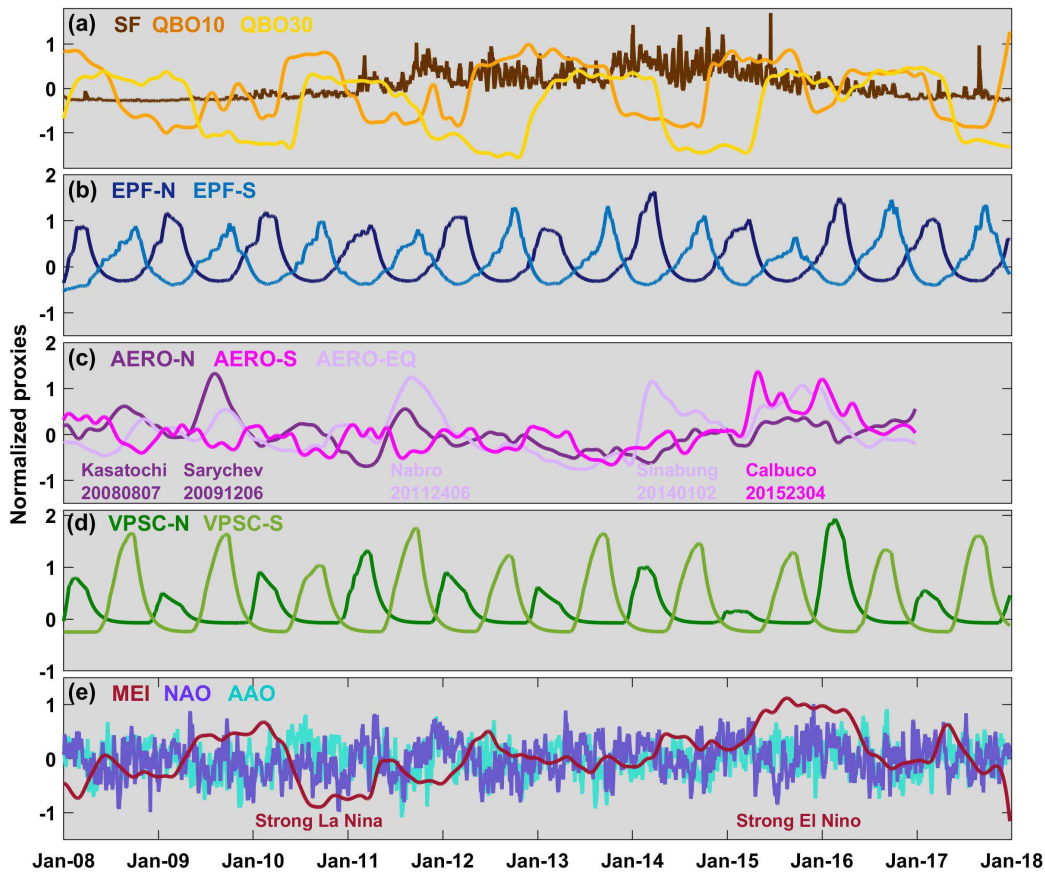


913

914 **Fig.1.** Global distribution of (a) daily O<sub>3</sub> columns (in Dobson Units - DU), (b) associated DOFS,  
 915 (c) absolute deseasonalized anomalies (in %) averaged over January 2008 – December 2017 in  
 916 the MUST (Mid-Upper Stratosphere: >25 hPa; left panels) and in the LSt (Lower Stratosphere:  
 917 150-25hPa; right panels). (d) shows the correlation coefficients between the daily O<sub>3</sub>  
 918 deseasonalized anomalies in the MUST and in the LSt. Note that the scales are different between  
 919 MUST and LSt.

920

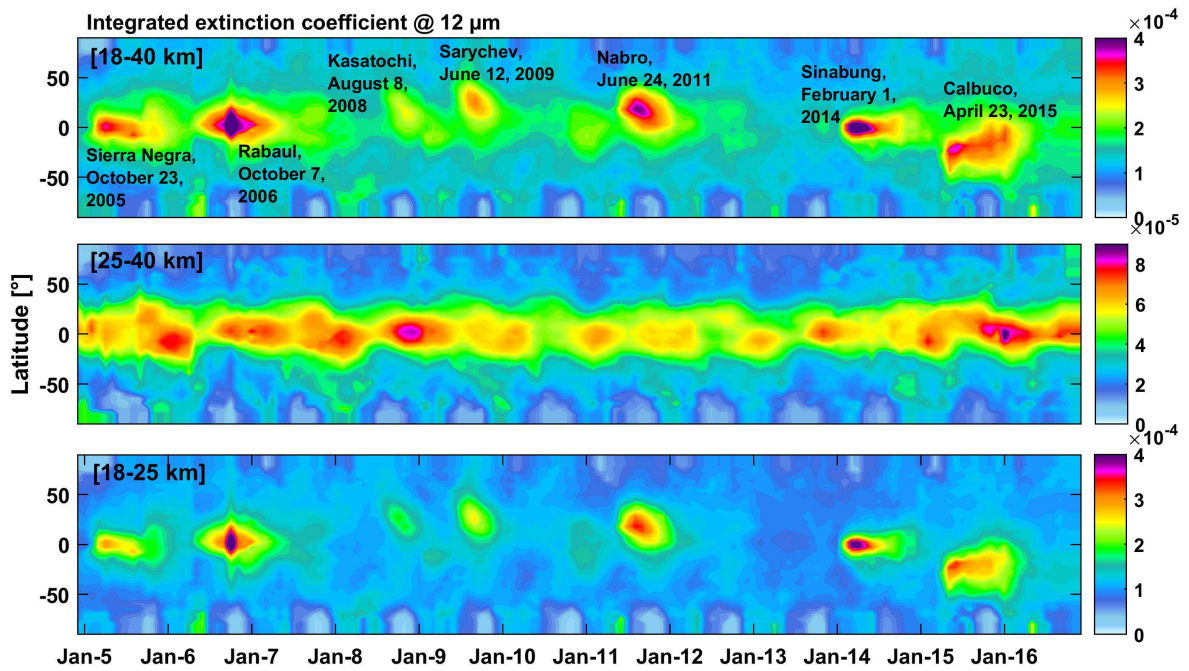
921



922  
 923  
 924  
 925  
 926  
 927  
 928  
 929  
 930  
 931  
 932  
 933  
 934  
 935  
 936

**Fig.2.** Normalized proxies as a function of time for the period covering January 2008 to December 2017 for (a) the F10.7 cm solar radio flux (SF) and the equatorial winds at 10 (QBO10) and 30 hPa (QBO30), respectively, (b) the upward components of the EP flux crossing 100 hPa accumulated over time and averaged over the 45°-75° latitude band for each hemispheres (EPF-N and EPF-S), (c) the extinction coefficients at 12 μm vertically integrated over the stratospheric O<sub>3</sub> column (from 150-2hPa) and averaged over the extra-tropics north and south (22.5°-90°N/S; AERO-N and AERO-S) and over the tropics (22.5°S-22.5°N; AERO-EQ) (the main volcanic eruptions are indicated), (d) the volume of polar stratospheric clouds multiplied by the equivalent effective stratospheric chlorine (EESC) and accumulated over time for the north and south hemispheres (VPSC-N and VPSC-S) and (e) the El Niño Southern (ENSO), North Atlantic (NAO) and Antarctic (AAO) oscillations.



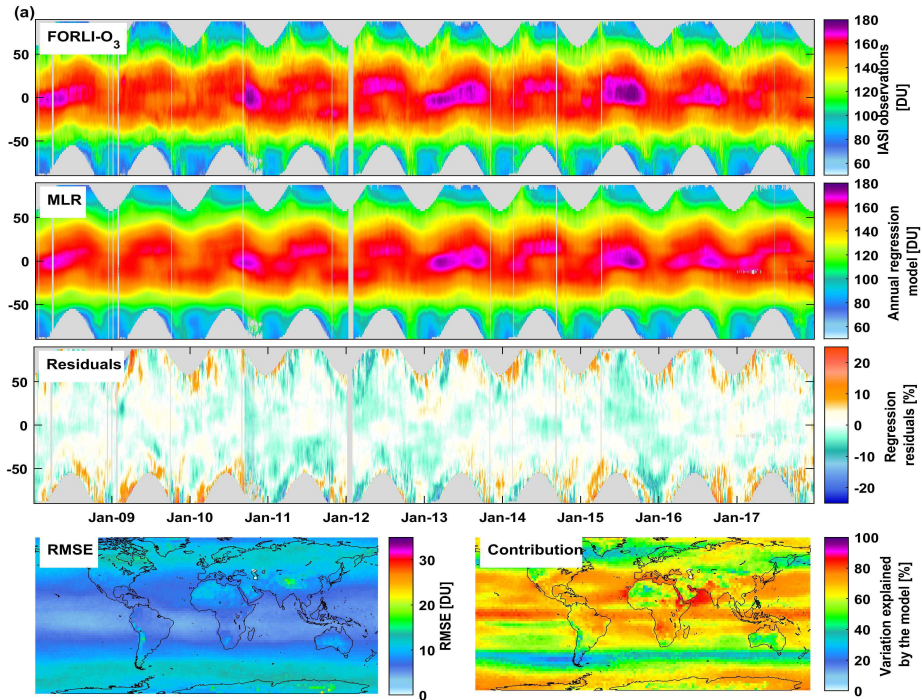


937  
938

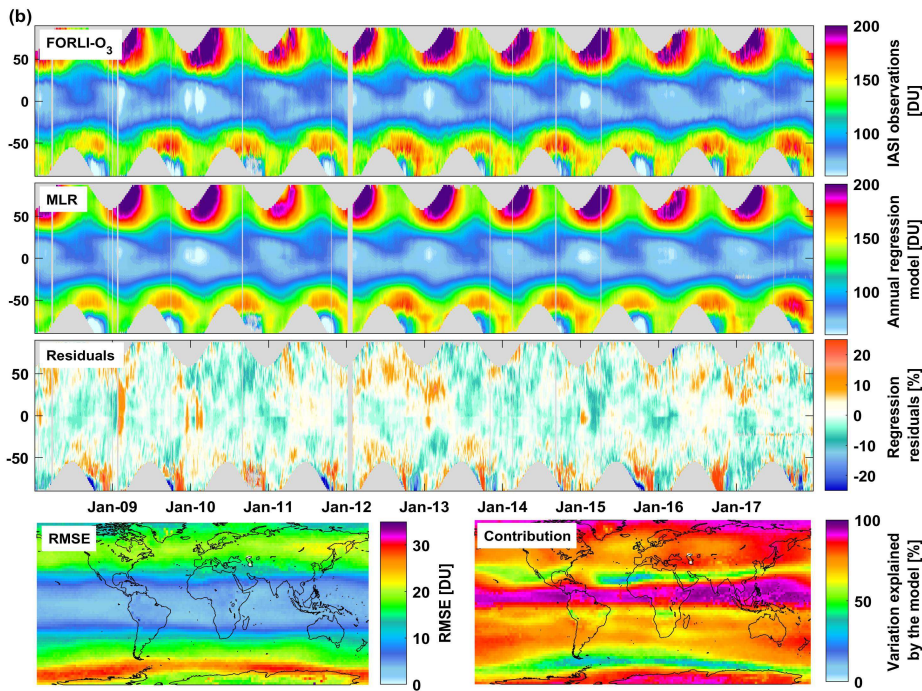
939 **Fig.3:** Latitudinal distribution of volcanic sulfuric acid extinction coefficient at 12  $\mu\text{m}$  integrated  
 940 over the stratosphere (top panel), over the middle stratosphere (middle panel) and the lower  
 941 stratosphere (bottom panel) as a function of time from 2005 to 2017. The dataset consists of  
 942 monthly mean aerosol data merged from SAGE, SAM, CALIPSO, OSIRIS, 2D-model-  
 943 simulation and Photometer (processed at NASA Langley Research Center, USA and ETH  
 944 Zurich, Switzerland).

945  
946  
947  
948  
949  
950  
951  
952  
953  
954  
955  
956  
957  
958  
959  
960  
961

962



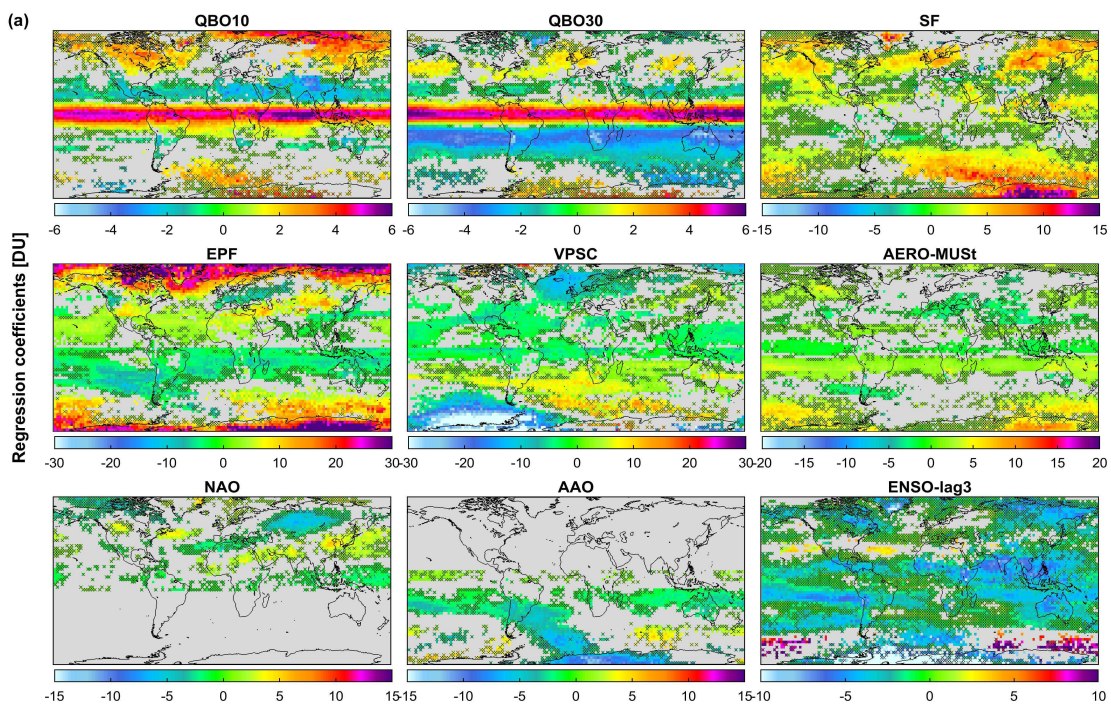
963  
964



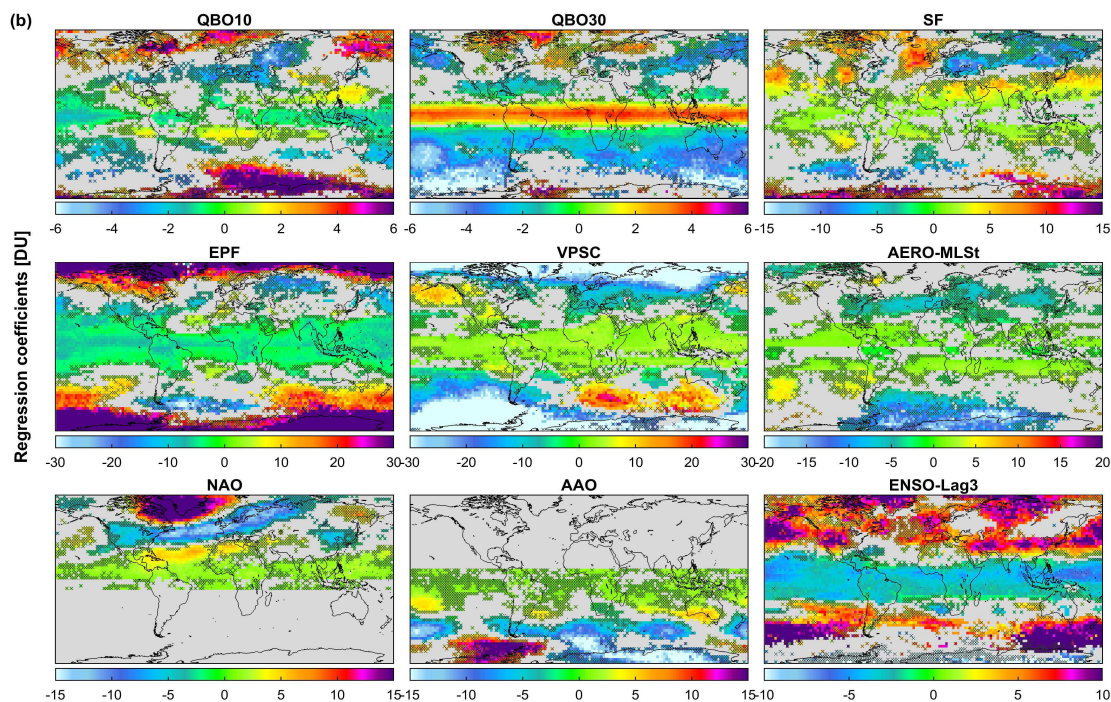
965 **Fig.4:** Latitudinal distribution of (a) MUST O<sub>3</sub> column and (b) LSt O<sub>3</sub> columns as a function of  
 966 time observed from IASI (in DU; top panels), simulated by the annual regression model (in DU,  
 967 second panels) and of the regression residuals (in %; third panels). Global distribution of *RMSE*  
 968 of the regression residual (in DU) and fraction of the variation in IASI data explained by the  
 969 regression model calculated as  $[100 \times (\sigma(O_3^{Fitted\_model}(t)) / \sigma(O_3(t)))]$  (in %; fourth panels).



970

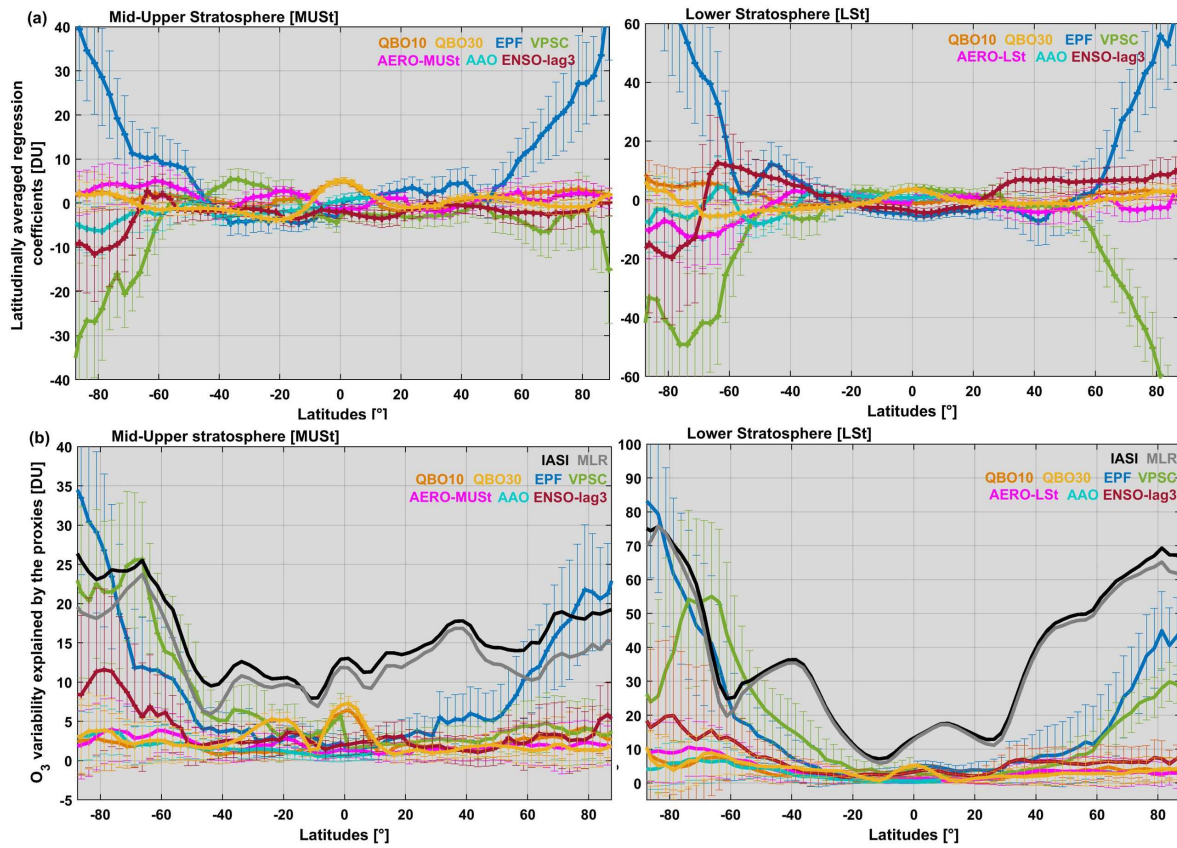


971



972

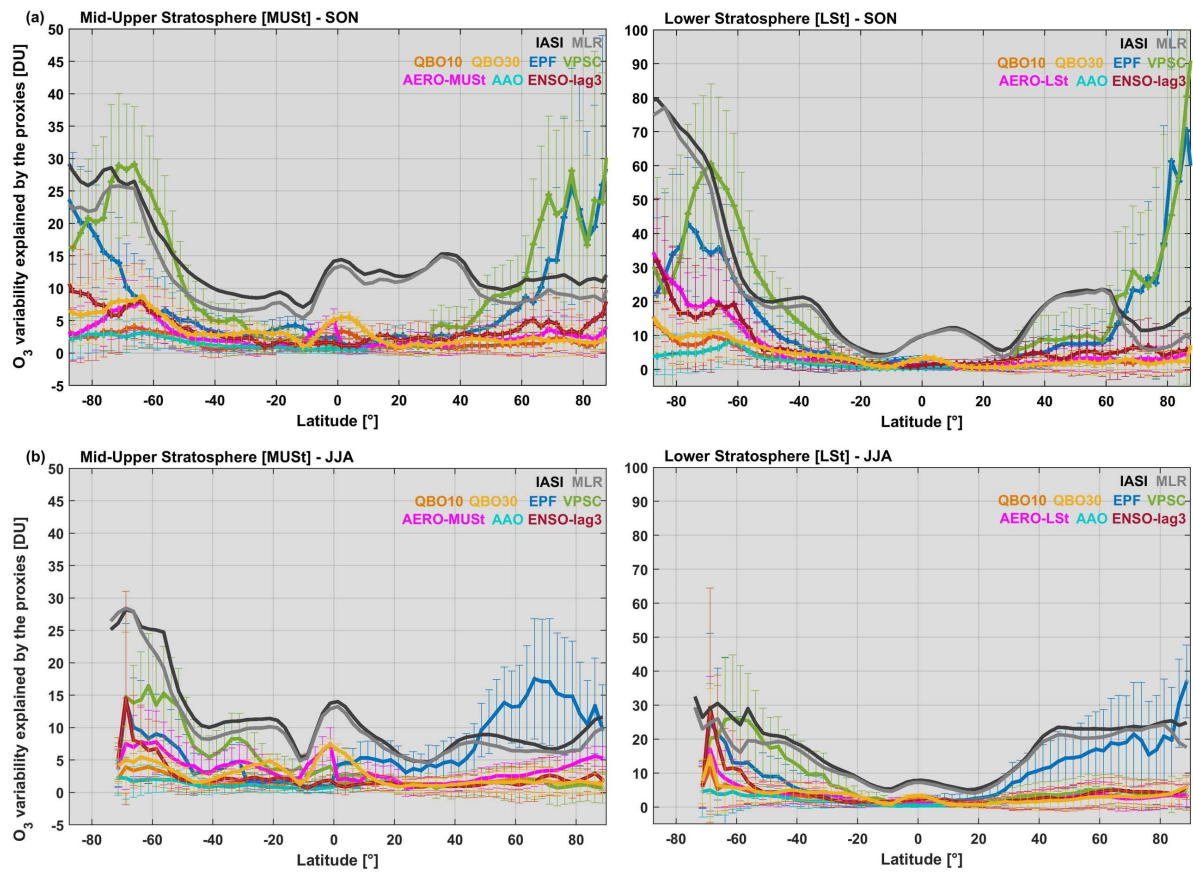
973 **Fig.5:** Global distribution of the annual regression coefficient estimates (in DU)  
974 drivers in (a) MUST and in (b) LSt: QBO10, QBO30, SF, EPF, VPSC, AERO, NAO, AAO and  
975 ENSO (ENSO-lag3 for both LSt and MUST). Grey areas and crosses refer to non-significant grid  
976 cells in the 95% confidence limit. Note that the scales differ among the drivers.



977  
 978  
 979  
 980  
 981  
 982  
 983  
 984  
 985  
 986  
 987  
 988  
 989

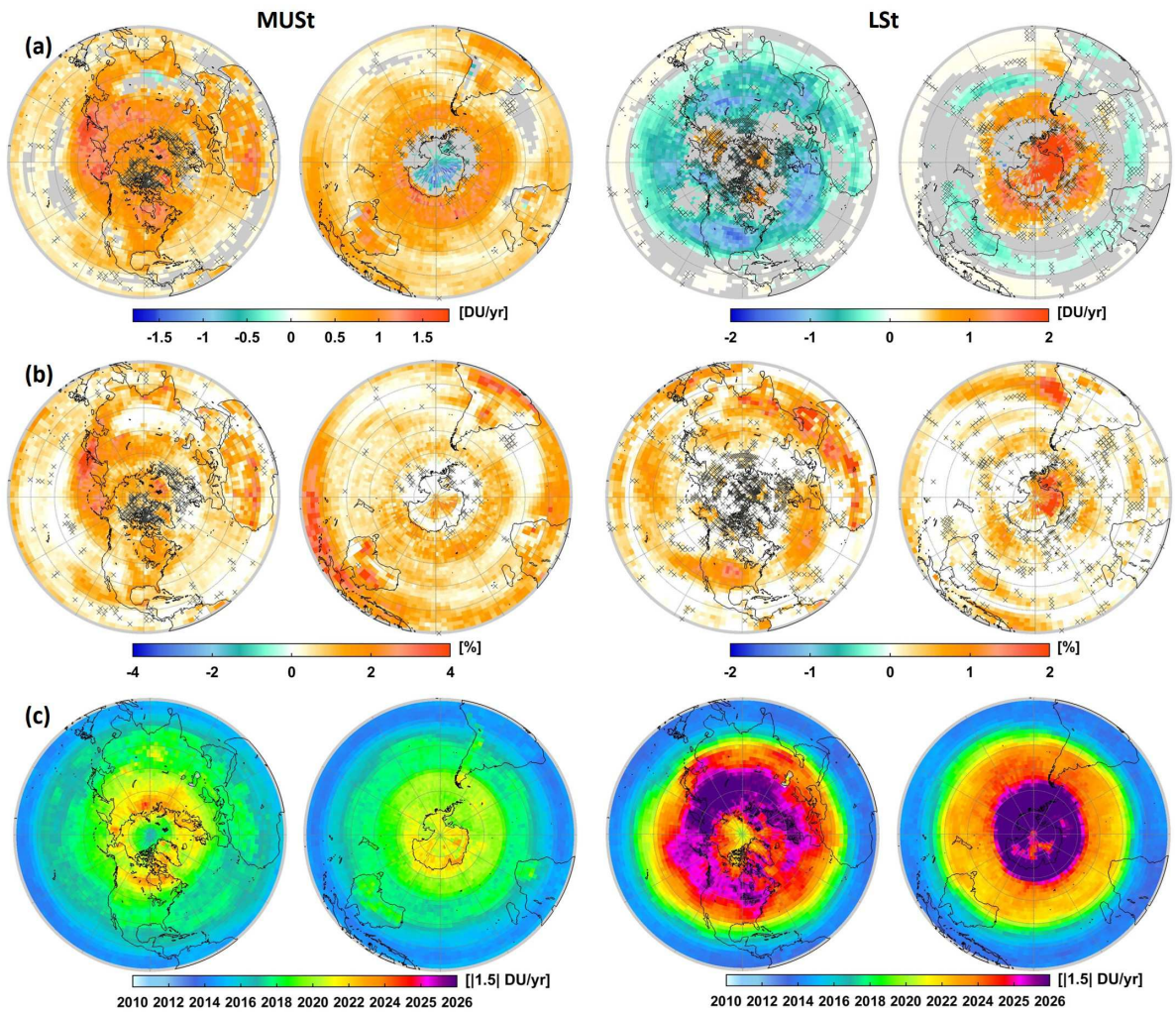
**Fig.6:** Latitudinal distributions (a) of fitting regression coefficients for various O<sub>3</sub> drivers (QBO10, QBO30, EPF, VPSC, AERO, AAO and ENSO-lag3; in DU) and (b) of 2 $\sigma$  O<sub>3</sub> variability due to variations in those drivers (in DU) from the annual MLR in MUST and LSt (left and right panels respectively). Vertical bars correspond (a) to the uncertainty of fitting coefficients at the 2 $\sigma$  level and (b) to the corresponding error contribution into O<sub>3</sub> variation. Note that the scales are different.





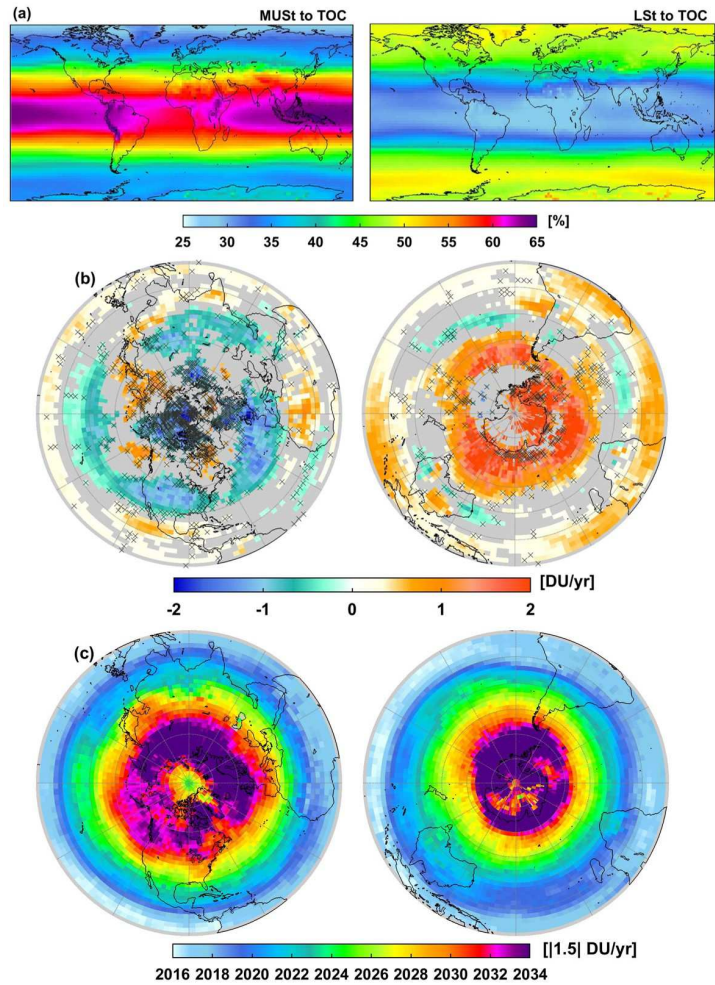
990  
 991  
 992  
 993  
 994  
 995

**Fig.7:** Same as Fig. 6b but for (a) the austral winter and (b) the austral spring periods (JJA and SON, respectively) from the seasonal MLR. Note that the scales are different.



996  
 997  
 998  
 999  
 1000  
 1001  
 1002  
 1003  
 1004  
 1005

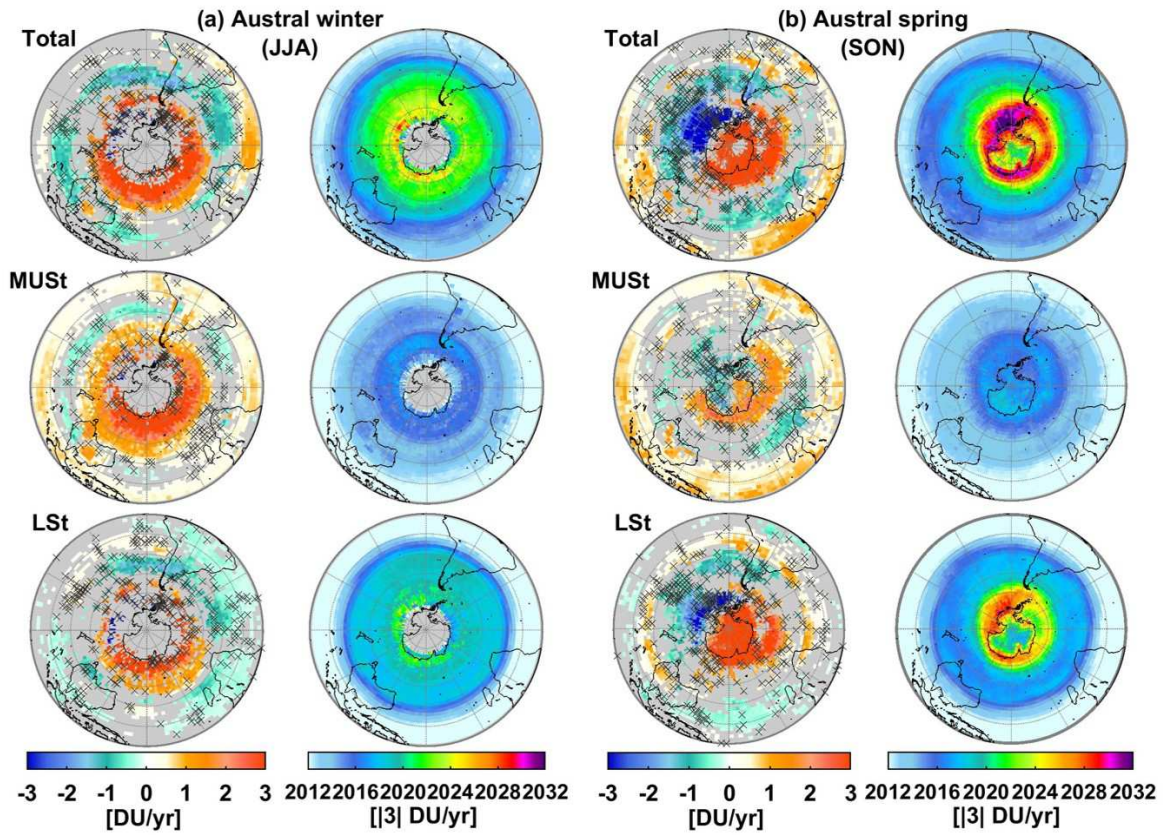
**Fig. 8:** Global distribution (a) of the estimated annual trends (in DU/yr; grey areas and crosses refer to non-significant grid cells in the 95% confidence limit), (b) of the IASI sensitivity to trend calculated as the differences between the *RMSE* of the annual MLR fits with and without linear trend term  $[(RMSE_{w/o\_LT} - RMSE_{with\_LT})/RMSE_{with\_LT} \times 100]$  (in %), (c) of the estimated year for a significant detection (with a probability of 90%) of a given trend of  $|1.5|$  DU/yr starting in January 2008 in MUST and LSt O<sub>3</sub> columns (left and right panels, respectively). Note that the scales are different for the two layers.



1006  
 1007  
 1008  
 1009  
 1010  
 1011  
 1012

**Fig.9:** Global distribution of (a) the contribution (in %) of MUST and LSt into the total O<sub>3</sub> (left and right panels respectively) averaged over January 2008 – December 2017, (b) fitted trends in total O<sub>3</sub> (in DU/yr; the grey areas and crosses refer to the non-significant grid cells in the 95% confidence limit) and (c) estimated year for the detection of a significant trend in total O<sub>3</sub> (with a probability of 90%) for a given trend of |1.5| DU/yr starting on January 2008.

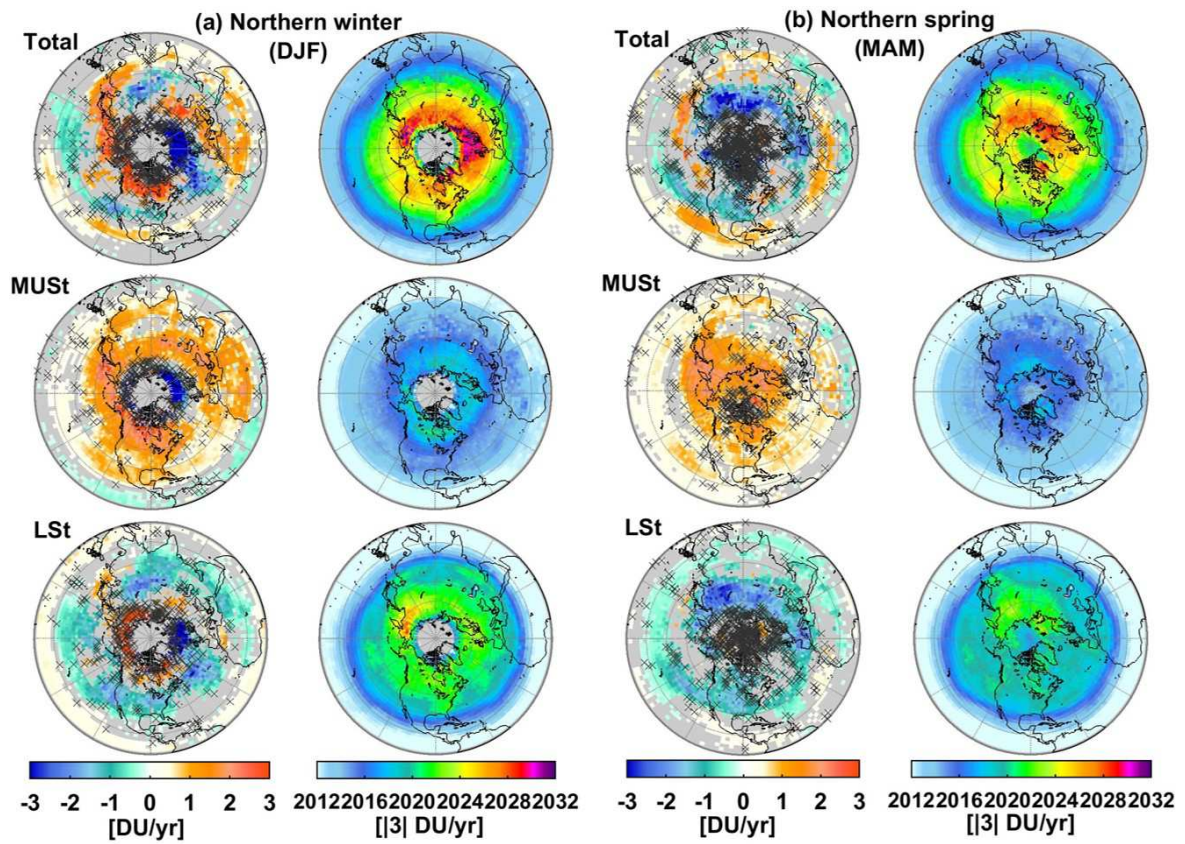




1013  
 1014  
 1015  
 1016  
 1017  
 1018  
 1019  
 1020  
 1021  
 1022  
 1023  
 1024  
 1025  
 1026  
 1027  
 1028  
 1029  
 1030  
 1031

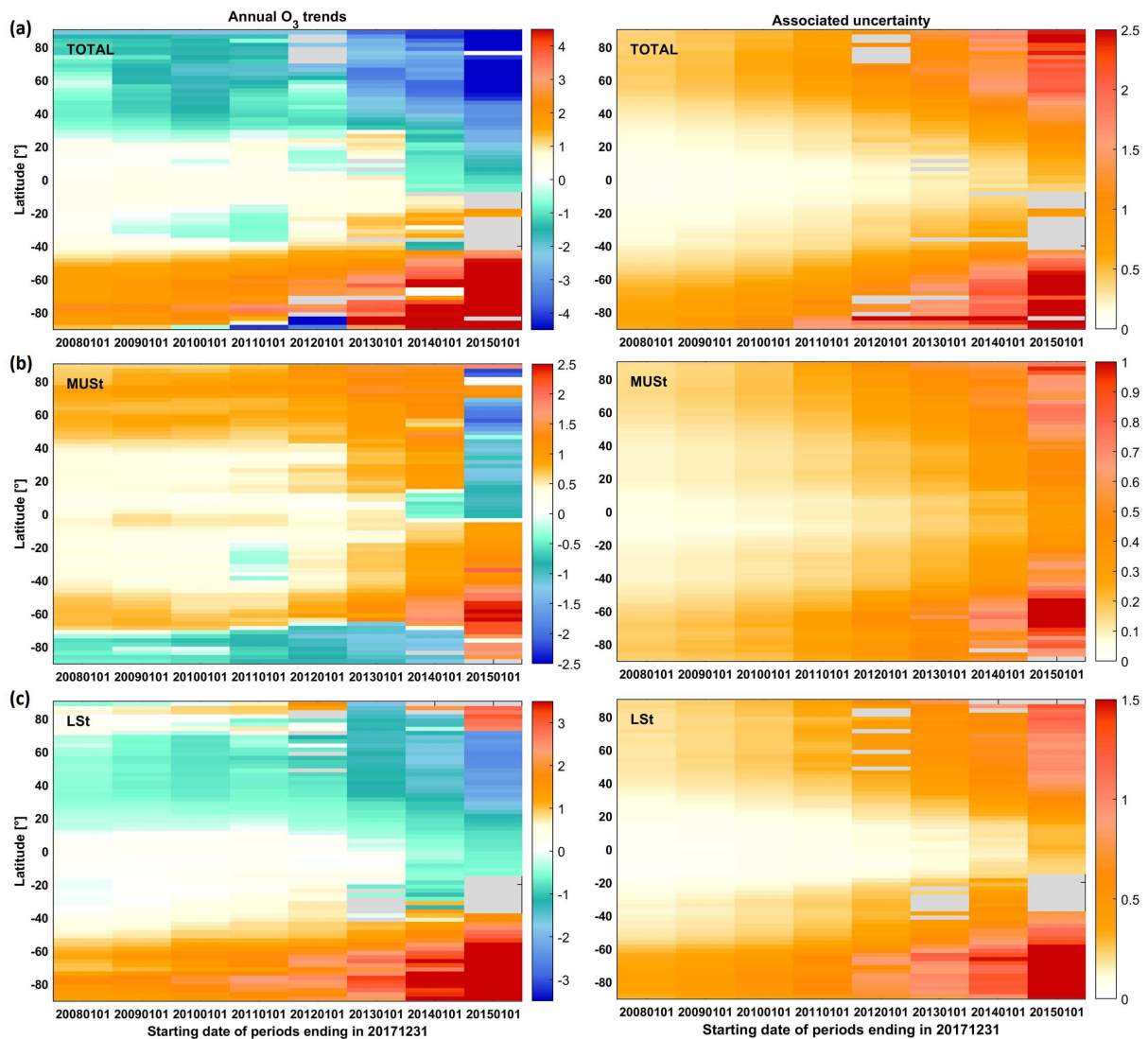
**Fig.10:** Hemispheric distribution (a) in austral winter (JJA) and (b) in austral spring (SON) of the estimated trends in total, MUSst and LSt O<sub>3</sub> columns (left panels: top, middle and bottom, respectively; in DU/yr; the grey areas and crosses refer to the non-significant grid cells in the 95% confidence limits) and of the corresponding estimated year for a significant trend detection (with a probability of 90%) of a given trend of  $|3|$  DU/yr starting at January 2008 (right panels: top, middle and bottom, respectively).





1032  
 1033  
 1034  
 1035  
 1036  
 1037  
 1038

**Fig. 11:** Same as Fig. 10 but (a) for the winter (DJF) and (b) for the spring (MAM) of the northern Hemisphere.



1039  
 1040 **Fig.12:** Evolution of estimated linear trend (DU/yr) and associated uncertainty accounting for the  
 1041 autocorrelation in the noise residuals (DU/yr; in the 95% confidence level) in (a) total, (b) MUSSt  
 1042 and (c) LSt O<sub>3</sub> columns, as a function of the covered IASI measurement period ending in  
 1043 December 2017, with all natural contributions estimated from the whole IASI period (2008-  
 1044 2017). Note that the scales are different between the columns.

1045  
 1046  
 1047  
 1048  
 1049  
 1050  
 1051  
 1052

1053 **References**

1054

1055 Anderson, J., Russell, J. M., Solomon, S., and Deaver, L. E.: Halogen Occultation Experiment  
1056 confirmation of stratospheric chlorine decreases in accordance with the Montreal Protocol, *J.*  
1057 *Geophys. Res.-Atmos.*, 105, 4483–4490, <https://doi.org/10.1029/1999JD901075>, 2000.

1058

1059 Baldwin, M. P., L.J. Gray, T.J. Dunkerton, K. Hamilton, P.H. Haynes, W.J. Randel, J.R. Holton,  
1060 M.J. Alexander, I. Hirota, T. Horinouchi, D.B.A. Jones, J.S. Kinnersley, C. Marquardt, K. Sato,  
1061 and M. Takahashi: The quasi-biennial oscillation, *Rev. Geophys.*, 39, 179–230,  
1062 doi:10.1029/1999RG000073, 2001.

1063

1064 Ball, W. T., Alsing, J., Mortlock, D. J., Staehelin, J., Haigh, J. D., Peter, T., Tummon, F., Stübi,  
1065 R., Stenke, A., Anderson, J., Bourassa, A., Davis, S. M., Degenstein, D., Frith, S., Froidevaux,  
1066 L., Roth, C., Sofieva, V., Wang, R., Wild, J., Yu, P., Ziemke, J. R., and Rozanov, E. V.:  
1067 Evidence for a continuous decline in lower stratospheric ozone offsetting ozone layer recovery,  
1068 *Atmos. Chem. Phys.*, 18, 1379–1394, <https://doi.org/10.5194/acp-18-1379-2018>, 2018.

1069

1070 Barnston, A. G. and Livezey, R. E.: Classification, seasonality and persistence of low-frequency  
1071 atmospheric circulation patterns, *Mon. Weather. Rev.* 115: 1083–1126, 1987.

1072

1073 Boynard, A., D. Hurtmans, K. Garane, F. Goutail, J. Hadji-Lazaro, M. E. Koukouli, C. Wespes,  
1074 C. Vigouroux, A. Keppens, J.-P. Pommereau, A. Pazmino, D. Balis, D. Loyola, P. Valks, R.  
1075 Sussmann, D. Smale, P.-F. Coheur and C. Clerbaux: Validation of the IASI FORLI/Eumetsat O<sub>3</sub>  
1076 products using satellite (GOME-2), ground-based (Brewer-Dobson, SAOZ, FTIR) and  
1077 ozonesonde measurements, *Atmos. Meas. Tech.*, 11, 5125–5152, 2018.

1078

1079 Brasseur, G.: The response of the middle atmosphere to long-term and short-term solar  
1080 variability: A two-dimensional model, *J. Geophys. Res.*, 98, 23 079–23 090, 1993.

1081

1082 Brönnimann, S., Luterbacher, J., Staehelin, J., Svendby, T. M., Hansen, G., and Svenøe, T.:  
1083 Extreme climate of the global troposphere and stratosphere 1940–1942 related to El Nino,  
1084 *Nature*, 431, 971–974, 2004.

1085

1086 Brunner, D., Staehelin, J., Maeder, J. A., Wohltmann, I., and Bodeker, G. E.: Variability and  
1087 trends in total and vertically resolved stratospheric ozone based on the CATO ozone data set,  
1088 *Atmos. Chem. Phys.*, 6, 4985–5008, doi:10.5194/acp-6-4985-2006, 2006.

1089

1090 Buffet, L., Villaret, C., Jacquette, E., Vandermarcq, O., Astruc, P., and Anstötz, S.: Status of  
1091 IASI instruments onboard Metop-A and Metop-B satellites, 4th IASI International Conference,  
1092 Antibes Juan-Les-Pins, France, 11–15 April 2016, available at:  
1093 [https://iasi.cnes.fr/sites/default/files/drupal/201612/default/bpc\\_iasi-conference4-](https://iasi.cnes.fr/sites/default/files/drupal/201612/default/bpc_iasi-conference4-1_02_instruments_buffet.pdf)  
1094 [1\\_02\\_instruments\\_buffet.pdf](https://iasi.cnes.fr/sites/default/files/drupal/201612/default/bpc_iasi-conference4-1_02_instruments_buffet.pdf) (last access: 30 August 2018), 2016.

1095

1096 Butler, A. H., M. Polvani, and C. Deser: Separating the stratospheric and tropospheric pathways  
1097 of El Niño–Southern Oscillation teleconnections, *Environ. Res. Lett.*, 9, 2, 024014,  
1098 doi:10.1088/1748-9326/9/2/024014, 2014.

1099

1100 Cagnazzo, C., E. Manzini, N. Calvo, A. Douglass, H. Akiyoshi, S. Bekki, M. Chipperfield, M.  
1101 Dameris, M. Deushi, A. M. Fischer, H. Garny, A. Gettelman, M. A. Giorgetta, D. Plummer, E.  
1102 Rozanov, T. G. Shepherd, K. Shibata, A. Stenke, H. Struthers and W. Tian: Northern winter  
1103 stratospheric temperature and ozone responses to ENSO inferred from an ensemble of Chemistry  
1104 Climate Models, *Atmos. Chem. Phys.*, 9, 8935–8948, [www.atmos-chem-phys.net/9/8935/2009/](http://www.atmos-chem-phys.net/9/8935/2009/),  
1105 2009.

1106

1107 Chabrillat, S., Vigouroux, C., Christophe, Y., Engel, A., Errera, Q., Minganti, D., Monge-Sanz,  
1108 B. M., Segers, A., and Mahieu, E.: Comparison of mean age of air in five reanalyses using the  
1109 BASCOE transport model, *Atmos. Chem. Phys.*, 18, 14715–14735, 2018.

1110

1111 Chipperfield, M. P., Kinnersley, J. S., and Zawodny, J.: A twodimensional model study of the  
1112 QBO signal in SAGE II NO<sub>2</sub> and O<sub>3</sub>, *Geophys. Res. Lett.*, 21, 589–592, 1994.

1113

1114 Chubachi, S.: Preliminary results of ozone observations at Syowa Station from February 1982 to  
1115 January 1983, in: *Proc. Sixth Symposium on Polar Meteorology and Glaciology*, edited by:  
1116 Kusunoki, K., vol. 34 of *Mem. National Institute of Polar Research Special Issue*, 13–19, 1984.

1117

1118 Clarisse, L., Clerbaux, C., Franco, B., Hadji-Lazaro, J., Whitburn, S., Kopp, A. K., D. Hurtmans  
1119 and P.-F. Coheur: A decadal data set of global atmospheric dust retrieved from IASI satellite  
1120 measurements, *J. Geophys. Res.*, 124, <https://doi.org/10.1029/2018JD029701>, 2019.

1121

1122 Coldewey-Egbers, M., D. G. Loyola R., P. Braesicke, M. Dameris, M. van Roozendaal, C. Lerot,  
1123 and W. Zimmer: A new health check of the ozone layer at global and regional scales, *Geophys.*  
1124 *Res. Lett.*, 41, 4363–4372, doi:10.1002/2014GL060212, 2014.

1125

1126 Clerbaux, C., A. Boynard, L. Clarisse, M. George, J. Hadji-Lazaro, H. Herbin, D. Hurtmans, M.  
1127 Pommier, A. Razavi, S. Turquety, C. Wespes, and P.-F. Coheur: Monitoring of atmospheric  
1128 composition using the thermal infrared IASI/MetOp sounder, *Atmos. Chem. Phys.*, 9, 6041–  
1129 6054, 2009.

1130

1131 Clerbaux, C. and Crevoisier, C.: New Directions: Infrared remote sensing of the troposphere  
1132 from satellite: Less, but better, *Atmos. Environ.*, 72, 24–26, 2013.

1133

1134 Cochran, D. and Orcutt, G. H.: Application of least squares regression to relationships  
1135 containing auto-correlated error terms, *J. Am. Stat. Assoc.*, 44, 32–61, 1949.

1136

1137 Crevoisier, C., Clerbaux, C., Guidard, V., Phulpin, T., Armante, R., Barret, B., Camy-Peyret, C.,  
1138 Chaboureaud, J.-P., Coheur, P.-F., Crépeau, L., Dufour, G., Labonnote, L., Lavanant, L., Hadji-  
1139 Lazaro, J., Herbin, H., Jacquinet-Husson, N., Payan, S., Péquignot, E., Pierangelo, C., Sellitto,  
1140 P., and Stubenrauch, C.: Towards IASI-New Generation (IASI-NG): impact of improved

1141 spectral resolution and radiometric noise on the retrieval of thermodynamic, chemistry and  
1142 climate variables, *Atmos. Meas. Tech.*, 7, 4367–4385, 2014.

1143

1144 Crutzen, P. J.: Estimates of possible future ozone reductions from continued use of fluoro-  
1145 chloro-methanes (CF<sub>2</sub>Cl<sub>2</sub>, CFC13), *Geophys. Res. Lett.*, 1, 205–208,  
1146 <https://doi.org/10.1029/GL001i005p00205>, 1974.

1147

1148 Dhomse, S., Weber, M., Wohltmann, I., Rex, M., and Burrows, J. P.: On the possible causes of  
1149 recent increases in northern hemispheric total ozone from a statistical analysis of satellite data  
1150 from 1979 to 2003, *Atm. Chem. Phys.*, 6, 1165–1180, 2006.

1151

1152 Dhomse, S. S., Chipperfield, P., Feng, W., Hossaini, R., Mann G. W., and Santee, M. L.:  
1153 Revisiting the hemispheric asymmetry in midlatitude ozone changes following the Mount  
1154 Pinatubo eruption: A 3-D model study, *Geophys. Res. Lett.*, 42, 3038–3047, 2015.

1155

1156 Domeisen, D. I., Garfinkel, C. I., and Butler, A. H.: The teleconnection of El Niño Southern  
1157 Oscillation to the stratosphere, *Reviews of Geophysics*, 57,  
1158 <https://doi.org/10.1029/2018RG000596>, 2019.

1159

1160 Errera, Q., S. Chabrillat, Y. Christophe, J. Debossher, D. Hubert, W. Lahoz, M. Santee, M.  
1161 Shiotani, S. Skachko, T. von Clarmann, and K. Walker: Reanalysis of Aura MLS Chemical  
1162 Observations submitted to *Atms. Chem. Phys. Discuss.*, doi:10.5194/acp-2019-530, 2019.

1163

1164 Farman, J. C., Gardiner, B. G., and Shanklin, J. D.: Large losses of total ozone in Antarctica  
1165 reveal seasonal ClO<sub>x</sub>/NO<sub>x</sub> interaction, *Nature*, 315, 207–210, doi:10.1038/315207a0, 1985.

1166

1167 Farmer, C. B., G. C. Toon, P. W. Shaper, J. F. Blavier, and L. L. Lowes, Stratospheric trace  
1168 gases in the spring 1986 Antarctic atmosphere, *Nature*, 329, 126–130, 1987.

1169

1170 Fioletov, V. E. and Shepherd, T. G.: Seasonal persistence of midlatitude total ozone anomalies,  
1171 *Geophys. Res. Lett.*, 30, 1417, doi:10.1029/2002GL016739, 2003.

1172

1173 Fioletov, V. E. and Shepherd, T. G.: Summertime total ozone variations over middle and polar  
1174 latitudes, *Geophys. Res. Lett.*, 32, 4807, doi:10.1029/2004GL022080, 2005.

1175

1176 Fishman, J., J.K. Creilson, A.E. Wozniak, and P.J. Crutzen, The interannual variability of  
1177 stratospheric and tropospheric ozone determined from satellite measurements, *J. Geophys. Res.*,  
1178 110, D20306, doi:10.1029/2005JD005868, 2005.

1179

1180 Frossard, L., H.E. Rieder, M. Ribatet, J. Staehelin, J. A. Maeder, S. Di Rocco, A. C. Davison, T.  
1181 Pete.: On the relationship between total ozone and atmospheric dynamics and chemistry at mid-  
1182 latitudes – Part 1: Statistical models and spatial fingerprints of atmospheric dynamics and  
1183 chemistry, *Atmos. Chem. Phys.*, 13, 147–164, doi:10.5194/acp-13-147-2013, 2013.

1184

1185 Fusco, A. C. and Salby, M. L.: Interannual variations of total ozone and their relationship to  
1186 variations of planetary wave activity, *J. Clim.*, 12, 1619–1629, 1999.  
1187

1188 Galytzka, E., Rozanov, A., Chipperfield, M. P., Dhomse, Sandip. S., Weber, M., Arosio, C.,  
1189 Feng, W., and Burrows, J. P.: Dynamically controlled ozone decline in the tropical mid-  
1190 stratosphere observed by SCIAMACHY, *Atmos. Chem. Phys.*, 19, 767-783,  
1191 <https://doi.org/10.5194/acp-19-767-2019>, 2019.  
1192

1193 Gebhardt, C., Rozanov, A., Hommel, R., Weber, M., Bovensmann, H., Burrows, J. P.,  
1194 Degenstein, D., Froidevaux, L., and Thompson, A. M.: Stratospheric ozone trends and variability  
1195 as seen by SCIAMACHY from 2002 to 2012, *Atmos. chem. Phys.*, 14, 831–846,  
1196 <https://doi.org/10.5194/acp-14-831-2014>, 2014.  
1197

1198 Harris, N. R. P., Hassler, B., Tummon, F., Bodeker, G. E., Hubert, D., Petropavlovskikh, I.,  
1199 Steinbrecht, W., Anderson, J., Bhartia, P. K., Boone, C. D., Bourassa, A., Davis, S. M.,  
1200 Degenstein, D., Delcloo, A., Frith, S. M., Froidevaux, L., Godin-Beekmann, S., Jones, N.,  
1201 Kurylo, M. J., Kyrölä, E., Laine, M., Leblanc, S. T., Lambert, J.-C., Liley, B., Mahieu, E.,  
1202 Maycock, A., De Mazière, M., Parrish, A., Querel, R., Rosenlof, K. H., Roth, C., Sioris, C.,  
1203 Staehelin, J., Stolarski, R. S., Stübi, R., Tamminen, J., Vigouroux, C., Walker, K. A., Wang, H.  
1204 J., Wild, J., and Zawodny, J. M.: Past changes in the vertical distribution of ozone – Part 3:  
1205 Analysis and interpretation of trends, *Atmos. Chem. Phys.*, 15, 9965-9982,  
1206 <https://doi.org/10.5194/acp-15-9965-2015>, 2015.  
1207

1208 Harrison, D. E., and Larkin, N. K.: El Niño-Southern Oscillation sea surface temperature and  
1209 wind anomalies, 1946–1993, *Rev. Geophys.*, 36, 353–399, doi:10.1029/98RG00715, 1998.  
1210

1211 Hilton, F., R. Armante, T. August, et al. : Hyperspectral Earth Observation from IASI: Five  
1212 Years of Accomplishments, *Bulletin of the American Meteorological Society*, vol. 93, issue 3,  
1213 pp. 347-370, 2012.  
1214

1215 Hofmann, D. J. and Solomon, S.: Ozone destruction through heterogeneous chemistry following  
1216 the eruption of El Chichón, *J. Geophys. Res.*, 94, 5029,  
1217 <https://doi.org/10.1029/JD094iD04p05029>, 1989.  
1218

1219 Hofmann, D. J., S. J. Oltmans, Antarctic ozone during 1992: Evidence for Pinatubo volcanic  
1220 aerosol effects. *J. Geophys. Res.* 98, 18555–18561, doi:10.1029/93JD02092, 1993.  
1221

1222 Hofmann, D. J., S. J. Oltmans, J. M. Harris, B. J. Johnson, and J. A. Lathrop: Ten years of  
1223 ozonesonde measurements at the south pole: Implications for recovery of springtime Antarctic  
1224 ozone, *J. Geophys. Res.*, 102(D7), 8931– 8943, doi:10.1029/96JD03749, 1997.  
1225

1226 Hood, L. L., McCormick, J. P., and Labitzke, K.: An investigation of dynamical contributions to  
1227 midlatitude ozone trends in winter, *J. Geophys. Res.*, 102, 13 079–13 093, 1997.  
1228



1229 Hood, L. L., and B. E. Soukharev: Quasi-decadal variability of the tropical lower stratosphere:  
1230 The role of extratropical wave forcing, *J. Atmos. Sci.*, 60, 2389–2403, 2003.  
1231

1232 Hood, L. L., and B. E. Soukharev: Solar induced variations of odd nitrogen: Multiple regression  
1233 analysis of UARS HALOE data, *Geophys. Res. Lett.*, doi:10.1029/2006GL028122, 2006.  
1234

1235 Hubert, D., Lambert, J.-C., Verhoelst, T., Granville, J., Keppens, A., Baray, J.-L., Bourassa, A.  
1236 E., Cortesi, U., Degenstein, D. A., Froidevaux, L., Godin-Beekmann, S., Hoppel, K. W.,  
1237 Johnson, B. J., Kyrölä, E., Leblanc, T., Lichtenberg, G., Marchand, M., McElroy, C. T.,  
1238 Murtagh, D., Nakane, H., Portafaix, T., Querel, R., Russell III, J. M., Salvador, J., Smit, H. G. J.,  
1239 Stebel, K., Steinbrecht, W., Strawbridge, K. B., Stübi, R., Swart, D. P. J., Taha, G., Tarasick, D.  
1240 W., Thompson, A. M., Urban, J., van Gijsel, J. A. E., Van Malderen, R., von der Gathen, P.,  
1241 Walker, K. A., Wolfram, E., and Zawodny, J. M.: Ground-based assessment of the bias and long-  
1242 term stability of 14 limb and occultation ozone profile data records, *Atmos. Meas. Tech.*, 9,  
1243 2497-2534, <https://doi.org/10.5194/amt-9-2497-2016>, 2016.  
1244

1245 Hurrell, J. W.: Decadal trends in the North Atlantic Oscillation regional temperatures and  
1246 precipitation, *Science*, 269, 676–679, 1995.  
1247

1248 Hurtmans, D., P. Coheur, C. Wespes, L. Clarisse, O. Scharf, C. Clerbaux, J. Hadji-Lazaro, M.  
1249 George, and S. Turquety: FORLI radiative transfer and retrieval code for IASI, *Journal of*  
1250 *Quantitative Spectroscopy and Radiative Transfer*, 113, 1391-1408, 2012.  
1251

1252 Jackman, C., E. Fleming, and F. Vitt: Influence of extremely large solar proton events in a  
1253 changing stratosphere, *J. Geophys. Res.*, 105, 11 659–11 670, 2000.  
1254

1255 Jonsson, A. I., de Grandpré, J., Fomichev, V. I., McConnell, J. C., and Beagley, S. R.: Doubled  
1256 CO<sub>2</sub>-induced cooling in the middle atmosphere: photochemical analysis of the ozone radiative  
1257 feedback, *J. Geophys. Res.*, 109, D24103, <https://doi.org/10.1029/2004JD005093>, 2004.  
1258

1259 Kalnay, E., M. Kanamitsu, R. Kistler, W. Collins, D. Deaven, L. Gandin, M. Iredell, S. Saha, G.  
1260 White, J. Woollen, Y. Zhu, M. Chelliah, W. Ebisuzaki, W. Higgins, J. Janowiak, K.C. Mo, C.  
1261 Ropelewski, J. Wang, A. Leetmaa, R. Reynolds, R. Jenne, and D. Joseph, 1996: The  
1262 NCEP/NCAR 40-Year Reanalysis Project. *Bull. Amer. Meteor. Soc.*, 77, 437–472,  
1263 <https://doi.org/10.1175/1520-0477>, 1996.  
1264

1265 Keeble, J., Brown, H., Abraham, N. L., Harris, N. R. P., and Pyle, J. A.: On ozone trend  
1266 detection: using coupled chemistry–climate simulations to investigate early signs of total column  
1267 ozone recovery, *Atmos. Chem. Phys.*, 18, 7625-7637, <https://doi.org/10.5194/acp-18-7625-2018>,  
1268 2018.  
1269

1270 Keppens, A., J.-C. Lambert, J. Granville, D. Hubert, T. Verhoelst, S. Compernelle, B. Latter, B.  
1271 Kerridge, R. Siddans, A. Boynard, J. Hadji-Lazaro, C. Clerbaux, C. Wespes, D. R. Hurtmans, P.-  
1272 F. Coheur, J. van Peet, R. van der A, K. Garane, M. E. Koukouli, D. S. Balis, A. Delcloo, R.  
1273 Kivi, R. Stübi, S. Godin-Beekmann, M. Van Roozendaal, C. Zehner: Quality assessment of the

1274 Ozone\_cci Climate Research Data Package (release 2017): 2. Ground-based validation of nadir  
1275 ozone profile data products, in preparation for this QOS special issue.  
1276

1277 Kyrölä, E., Laine, M., Sofieva, V., Tamminen, J., Päivärinta, S.-M., Tukiainen, S., Zawodny, J.,  
1278 and Thomason, L.: Combined SAGE II-GOMOS ozone profile data set for 1984–2011 and trend  
1279 analysis of the vertical distribution of ozone, *Atmos. Chem. Phys.*, 13, 10645–10658,  
1280 <https://doi.org/10.5194/acp-13-10645-2013>, 2013.  
1281

1282 Kodera, K. and Kuroda, Y.: Dynamical response to the solar cycle: Winter stratopause and lower  
1283 stratosphere, *J. Geophys. Res.*, 107, 4749, doi:310.1029/2002JD002224, 2002.  
1284

1285 Kuttippurath, J., F. Lefèvre, J.-P. Pommereau, H. K. Roscoe, F. Goutail, A. Pazmiño, J. D.  
1286 Shanklin, Antarctic ozone loss in 1979–2010: First sign of ozone recovery. *Atmos. Chem. Phys.*  
1287 13, 1625–1635, doi:10.5194/acp-13-1625-2013, 2013.  
1288

1289 Kuttippurath, J., and P.J. Nair: The signs of Antarctic ozone hole recovery 2017, *Scientific*  
1290 *Reports*, 7, 585, doi:10.1038/s41598-017-00722-7, 2017.  
1291

1292 [Kuttippurath, J., P. Kumar, P.J. Nair, P.C. Pandey: Emergence of ozone recovery evidenced by](#)  
1293 [reduction in the occurrence of Antarctic ozone loss saturation, \*Climate and Atmospheric Science\*,](#)  
1294 [1, 42, 2397-3722, doi: 10.1038/s41612-018-0052-6, 2018.](#)  
1295

1296 Labitzke, K. and van Loon, H.: The QBO effect on the solar signal in the global stratosphere in  
1297 the winter of the Northern Hemisphere, *J. Atmos. Solar-Terr. Phys.*, 62, 621–628, 2000.  
1298

1299 Mäder, J. A., J. Staehelin, D. Brunner, W.A. Stahel, I. Wohltmann, and T. Peter: Statistical  
1300 modelling of total ozone: Selection of appropriate explanatory variables, *J. Geophys. Res.*, 112,  
1301 D11108, doi:10.1029/2006JD007694, 2007.  
1302

1303 Mäder, J. A., J. Staehelin, T. Peter, D. Brunner, H. E. Rieder, and W. A. Stahel: Evidence for the  
1304 effectiveness of the Montreal Protocol to protect the ozone layer, *Atmos. Chem. Phys.*, 10, 24,  
1305 12,161–12,171, doi:10.5194/acp-10-12161-2010, 2010.

1306 Manatsa, D. and G. Mukwada: A connection from stratospheric ozone to El Niño-Southern  
1307 Oscillation, *Scientific Reports*, 7, 5558, DOI:10.1038/s41598-017-05111-8, 2017.

1308 Manzini, E., Giorgetta, M. A., Esch, M., Kornblueh, L., and Roeckner, E.: The influence of sea  
1309 surface temperatures on the northern winter stratosphere: Ensemble simulations with the  
1310 MAECHAM5 model, *J. Climate*, 19, 3863–3881, 2006.  
1311

1312 McCormack, J. P., D. E. Siskind, and L. L. Hood: Solar-QBO interaction and its impact on  
1313 stratospheric ozone in a zonally averaged photochemical transport model of the middle  
1314 atmosphere, *J. Geophys. Res.*, 112, D16109, doi:10.1029/2006JD008369, 2007.  
1315

1316 McPeters, R. D., G.J. Labow, and J.A. Logan: Ozone climatological profiles for satellite retrieval  
1317 algorithms, *J. Geophys. Res.-Atmos.*, 112, D05308, doi:10.1029/2005JD006823, 2007.  
1318

1319 Molina, M. J. and Rowland, F. S.: Stratospheric sink for chlorofluoromethanes: Chlorine atom-  
1320 catalysed destruction of ozone, *Nature*, 249, 810–812, 1974.  
1321

1322 Nair, P. J., Froidevaux, L., Kuttippurath, J., Zawodny, J. M., Russell, J. M., Steinbrecht, W.,  
1323 Claude, H., Leblanc, T., van Gijssel, J. A. E., Johnson, B., Swart, D. P. J., Thomas, A., Querel, R.,  
1324 Wang, R., and Anderson, J.: Subtropical and midlatitude ozone trends in the stratosphere:  
1325 Implications for recovery, *J. Geophys. Res.-Atmos.*, 120, 7247–7257,  
1326 <https://doi.org/10.1002/2014JD022371>, 2015.  
1327

1328 Newchurch, M. J., Yang, E.-S., Cunnold, D. M., Reinsel, G. C., Zawodny, J. M., and Russell III,  
1329 J. M.: Evidence for slowdown in stratospheric ozone loss: First stage of ozone recovery, *J.*  
1330 *Geophys. Res.*, 108, 4507, doi:10.1029/2003JD003471, 2003.  
1331

1332 Newman, P. A., Nash, E. R., Kawa, S. R., Montzka, S. A., and Schauffler, S. M.: When will the  
1333 Antarctic ozone hole recover?: *Geophys. Res. Lett.*, 33, L12814, doi:10.1029/2005GL025232,  
1334 2006.  
1335

1336 Oman, L. D., Douglass, A. R., Ziemke, J. R., Rodriguez, J. M., Waugh, D. W., and Nielsen, J.  
1337 E.: The ozone response to ENSO in Aura satellite measurements and a chemistry–climate  
1338 simulation, *J. Geophys. Res.-Atmos.*, 118, 965–976, 2013.  
1339

1340 Pawson, S., Steinbrecht, W., Charlton-Perez, A J Fujiwara, M., Karpechko, A. Y.,  
1341 Petropavlovskikh, I., Urban, J., and Weber, M.: Update on Global Ozone: Past, Present, and  
1342 Future, in: *Scientific Assessment of Ozone Depletion: 2014*, World Meteorological  
1343 Organization, Global Ozone Research and Monitoring Project – Report No. 55, chap. 2, World  
1344 Meteorological Organization/UNEP, 2014.  
1345

1346 Portmann, R. W., S. Solomon, R. R. Garcia, L. W. Thomason, L. R. Poole, M. P. McCormick,  
1347 Role of aerosol variations in anthropogenic ozone depletion in the polar regions. *J. Geophys.*  
1348 *Res.* 101, 22991–23006, doi:10.1029/96JD02608, 1996.  
1349

1350 Knudsen, B. M. and Grooss, J.: Northern midlatitude stratospheric ozone dilution in spring  
1351 modeled with simulated mixing, *J. Geophys. Res.*, 105, 6885–6890, 2000.  
1352

1353 Randel, W. J. and Cobb, J. B.: Coherent variations of monthly mean total ozone and lower  
1354 stratospheric temperature, *J. Geophys. Res.-Atmos.*, 99, 5433–5447, 1994.  
1355

1356 Randel, W. J. and F. Wu: Isolation of the ozone QBO in SAGE II data by singular-value  
1357 decomposition, *J. Atmos. Sci.*, 53, 2546– 2559, 1996.  
1358

1359 Randel, W. J., F. Wu, and R. Stolarski: Changes in column ozone correlated with the  
1360 stratospheric EP flux, *J. Meteorol. Soc. Jpn.*, 80, 849–862, 2002.

1361  
1362 Randel, W. J., Garcia, R. R., Calvo, N., and Marsh, D.: ENSO influence on zonal mean  
1363 temperature and ozone in the tropical lower stratosphere, *Geophys. Res. Lett.*, 36, L15822,  
1364 <https://doi.org/10.1029/2009GL039343>, 2009.  
1365  
1366 Randel, W. J., and A. M. Thompson: Interannual variability and trends in tropical ozone derived  
1367 from SAGE II satellite data and SHADOZ ozonesondes, *J. Geophys. Res.*, 116, D07303,  
1368 doi:10.1029/2010JD015195, 2011.  
1369  
1370 Reinsel, G. C., Miller, A. J., Weatherhead, E. C., Flynn, L. E., Nagatani, R. M., Tiao, G. C., and  
1371 Wuebbles, D. J.: Trend analysis of total ozone data for turnaround and dynamical contributions,  
1372 *J. Geophys. Res.*, 110, D16306, doi:10.1029/2004JD004662, 2005.  
1373  
1374 Revell, L. E., Stenke, A., Luo, B., Kremser, S., Rozanov, E., Sukhodolov, T., and Peter, T.:  
1375 Impacts of Mt Pinatubo volcanic aerosol on the tropical stratosphere in chemistry–climate model  
1376 simulations using CCM1 and CMIP6 stratospheric aerosol data, *Atmos. Chem. Phys.*, 17, 13139–  
1377 13150, 2017.  
1378  
1379 Rex, M., Salawitch, R. J., von der Gathen, P., Harris, N. R. P., Chipperfield, M. P., and  
1380 Naujokat, B.: Arctic ozone loss and climate change, *Geophys. Res. Lett.*, 32, L04116,  
1381 doi:10.1029/2003GL018844, 2004.  
1382  
1383 Rieder, H. E., Frossard, L., Ribatet, M., Staehelin, J., Maeder, J. A., Di Rocco, S., Davison, A.  
1384 C., Peter, T., Weihs, P., and Holawe, F.: On the relationship between total ozone and atmospheric  
1385 dynamics and chemistry at mid-latitudes – Part 2: The effects of the El Niño/Southern  
1386 Oscillation, volcanic eruptions and contributions of atmospheric dynamics and chemistry to  
1387 long-term total ozone changes, *Atmos. Chem. Phys.*, 13, 165–179, 2013.  
1388  
1389 Rind, D., Perlwitz, J., and Lonergan, P.: AO/NAO response to climate change: 1. Respective  
1390 influences of stratospheric and tropospheric climate changes, *J. Geophys. Res.*, 110, D12107,  
1391 doi: 10.1029/2004JD005103, 2005.  
1392  
1393 Rodgers, C. D.: *Inverse Methods for Atmospheric Sounding: Theory and Practice*, World  
1394 Scientific, Series on Atmospheric, Oceanic and Planetary Physics, 2, Hackensack, N. J., 2000.  
1395  
1396 [Roscoe, H. K. and Haigh, J. D.: Influences of ozone depletion, the solar cycle and the QBO on](#)  
1397 [the Southern Annular Mode, \*Q. J. Roy. Met. Soc.\*, 133, 1855–1864, 2007.](#)  
1398  
1399 Salby, M., E. Titova, and L. Deschamps: Rebound of Antarctic ozone, *Geophys. Res. Lett.*, 38,  
1400 L09702, doi:10.1029/2011GL047266, 2011.  
1401  
1402 Schnadt, C. and Dameris, M.: Relationship between North Atlantic Oscillation changes and  
1403 stratospheric ozone recovery in the Northern Hemisphere in a chemistry-climate model, *J.*  
1404 *Geophys. Res.*, 30, 1487, doi:10.1029/2003GL017006, 2003.  
1405

1406 Shepherd, T. G., Plummer, D. A., Scinocca, J. F., Hegglin, M. I., Fioletov, V. E., Reader, M. C.,  
1407 Remsberg, E., von Clarmann, T., and Wang, H. J.: Reconciliation of halogen-induced ozone loss  
1408 with the total-column ozone record, *Nat. Geosci.*, 7, 443–449, <https://doi.org/10.1038/ngeo2155>,  
1409 2014.

1410

1411 Sioris, C. E., McLinden, C. A., Fioletov, V. E., Adams, C., Zawodny, J. M., Bourassa, A. E.,  
1412 Roth, C. Z., and Degenstein, D. A.: Trend and variability in ozone in the tropical lower  
1413 stratosphere over 2.5 solar cycles observed by SAGE II and OSIRIS, *Atmos. Chem. Phys.*, 14,  
1414 3479–3496, <https://doi.org/10.5194/acp-14-3479-2014>, 2014.

1415

1416 Sofieva, V. F., Kyrölä, E., Laine, M., Tamminen, J., Degenstein, D., Bourassa, A., Roth, C.,  
1417 Zawada, D., Weber, M., Rozanov, A., Rahpoe, N., Stiller, G., Laeng, A., von Clarmann, T.,  
1418 Walker, K. A., Sheese, P., Hubert, D., van Roozendaal, M., Zehner, C., Damadeo, R., Zawodny,  
1419 J., Kramarova, N., and Bhartia, P. K.: Merged SAGE II, Ozone\_cci and OMPS ozone profile  
1420 dataset and evaluation of ozone trends in the stratosphere, *Atmos. Chem. Phys.*, 17, 12533–  
1421 12552, <https://doi.org/10.5194/acp-17-12533-2017>, 2017.

1422

1423 Solomon, S., R. R. Garcia, F. S. Rowland, and D. J. Wuebbles, On the depletion of Antarctic  
1424 zone, *Nature*, 321, 755–758, 1986.

1425

1426 Solomon, S., Portman, R. W., Garcia, R. R., Thomason, L. W., Poole, L. R., and McCormack,  
1427 M. P.: The role of aerosol variations in anthropogenic ozone depletion at northern midlatitudes,  
1428 *J. Geophys. Res.*, 101, 6713–6727, 1996.

1429

1430 Solomon, S.: Stratospheric ozone depletion: A review of concepts and history. *Rev. Geophys.*  
1431 37, 275–316, doi:10.1029/1999RG900008, 1999.

1432

1433 Solomon, P., Barrett, J., Mooney, T., Connor, B., Parrish, A., and Siskind, D. E.: Rise and  
1434 decline of active chlorine in the stratosphere, *Geophys. Res. Lett.*, 33, L18807,  
1435 <https://doi.org/10.1029/2006GL027029>, 2006.

1436

1437 Solomon, S., Ivy, D. J., Kinnison, D., Mills, M. J., Neely, R. R., and Schmidt, A.: Emergence of  
1438 healing in the Antarctic ozone layer, *Science*, 353, 269–274,  
1439 <https://doi.org/10.1126/science.aae0061>, 2016.

1440

1441 Stolarski, R. S., A. J. Krueger, M. R. Schoeberl, R. D. Mc-Peters, P. A. Newman, and J. C.  
1442 Alpert, Nimbus 7 satellite measurements of the springtime Antarctic ozone decrease, *Nature*,  
1443 322, 808–811, 1986.

1444

1445 Soukharev, B. E. and L. L. Hood: Solar cycle variation of stratospheric ozone: Multiple  
1446 regression analysis of long-term satellite data sets and comparisons with models, *J. Geophys.*  
1447 *Res.*, 111, D20314, doi:10.1029/2006JD007107, 2006.

1448

1449 Steinbrecht, W., H. Claude, U. Köhler, and K. P. Hoinka: Correlations between tropopause  
1450 height and total ozone: Implications for long-term changes, *J. Geophys. Res.*, *103*, 19,183–  
1451 19,192, doi:10.1029/98JD01929, 1998.

1452

1453 Steinbrecht, W., B. Hassler, H. Claude, P. Winkler, and R. S. Stolarski: Global distribution of  
1454 total ozone and lower stratospheric temperature variations, *Atmos. Chem. Phys.*, *3*, 1421–1438,  
1455 2003.

1456

1457 Steinbrecht, W., et al.: Interannual variation patterns of total ozone and lower stratospheric  
1458 temperature in observations and model simulations, *Atmos. Chem. Phys.*, *6*, 349–374,  
1459 doi:10.5194/acp-6-349-2006, 2006

1460

1461 Steinbrecht, W., Froidevaux, L., Fuller, R., Wang, R., Anderson, J., Roth, C., Bourassa, A.,  
1462 Degenstein, D., Damadeo, R., Zawodny, J., Frith, S., McPeters, R., Bhartia, P., Wild, J., Long,  
1463 C., Davis, S., Rosenlof, K., Sofieva, V., Walker, K., Ralpoe, N., Rozanov, A., Weber, M.,  
1464 Laeng, A., von Clarmann, T., Stiller, G., Kramarova, N., Godin-Beekmann, S., Leblanc, T.,  
1465 Querel, R., Swart, D., Boyd, I., Hocke, K., Kämpfer, N., Maillard Barras, E., Moreira, L.,  
1466 Nedoluha, G., Vigouroux, C., Blumenstock, T., Schneider, M., García, O., Jones, N., Mahieu, E.,  
1467 Smale, D., Kotkamp, M., Robinson, J., Petropavlovskikh, I., Harris, N., Hassler, B., Hubert, D.,  
1468 and Tummon, F.: An update on ozone profile trends for the period 2000 to 2016, *Atmos. Chem.*  
1469 *Phys.*, *17*, 10675–10690, doi:10.5194/acp-17-10675-2017, 2017.

1470

1471 Thomason, L. W., Ernest, N., Millán, L., Rieger, L., Bourassa, A., Vernier, J.-P., Manney, G.,  
1472 Luo, B., Arfeuille, F., and Peter, T.: A global space-based stratospheric aerosol climatology:  
1473 1979–2016, *Earth Syst. Sci. Data*, *10*, 469-492, <https://doi.org/10.5194/essd-10-469-2018>, 2018.

1474

1475 Thompson, D. W. J. and J.M. Wallace: Annular modes in the extratropical circulation. Part I:  
1476 month-to-month variability, *J. Climate*, *13*, 1000–1016, 2000.

1477

1478 Thompson, D. W. J. and Solomon, S.: Interpretation of Recent Southern Hemisphere Climate  
1479 Change, *Science*, *296*, 895-899, 2002.

1480

1481 Tian, W., M.P. Chipperfield, L.J. Gray, and J.M. Zawodny: Quasi-biennial oscillation and tracer  
1482 distributions in a coupled chemistry-climate model, *J. Geophys. Res.*, *111*, D20301,  
1483 doi:10.1029/2005JD006871, 2006.

1484

1485 Tiao, G. C., G. C. Reinsel, D. Xu, J. H. Pedrick, X. Zhu, A. J. Miller, J. J. DeLuisi, C. L. Mateer,  
1486 and D. J. Wuebbles, Effects of autocorrelation and temporal sampling schemes on estimates of  
1487 trend and spatial correlation, *J. Geophys Res.*, *95*, 20,507-20,517, 1990.

1488

1489 Tweedy, O. V., Waugh, D. W., Randel, W. J., Abalos, M., Oman, L. D. and Kinnison, D. E.: The  
1490 impact of boreal summer ENSO events on tropical lower stratospheric ozone, *J. Geophys. Res.*,  
1491 *Atmospheres*, *123*, 9843–9857, doi:10.1029/2018JD029020, 2018.

1492



1493 Valks, P., N. Hao, S. Gimeno Garcia, D. Loyola, M. Dameris, P. Jöckel, and A. Delcloo:  
1494 Tropical tropospheric ozone column retrieval for GOME-2, *Atmos. Meas. Tech.*, 7, 2513–2530,  
1495 doi:10.5194/amt-7-2513-2014, 2014.  
1496  
1497 Vigouroux, C., Blumenstock, T., Coffey, M., Errera, Q., García, O., Jones, N. B., Hannigan, J.  
1498 W., Hase, F., Liley, B., Mahieu, E., Mellqvist, J., Notholt, J., Palm, M., Persson, G., Schneider,  
1499 M., Servais, C., Smale, D., Thölix, L., and De Mazière, M.: Trends of ozone total columns and  
1500 vertical distribution from FTIR observations at eight NDACC stations around the globe, *Atmos.*  
1501 *Chem. Phys.*, 15, 2915–2933, <https://doi.org/10.5194/acp-15-2915-2015>, 2015.  
1502  
1503 Weatherhead, E.C., G. C. Reinsel, G. C. Tiao, X.-L. Meng, D. Choi, W.-K. Cheang, T. Keller, J.  
1504 DeLuisi, D. J. Wuebbles, J. B. Kerr, A. J. Miller, S. J. Oltmans and J. E. Frederick: Factors  
1505 affecting the detection of trends: Statistical considerations and applications to environmental  
1506 data, *J. Geophys. Res. Atmos.*, 103, 17149–17161, 1998.  
1507  
1508 Weber, M., Dikty, S., Burrows, J. P., Garny, H., Dameris, M., Kubin, A., Abalichin, J., and  
1509 Langematz, U.: The Brewer-Dobson circulation and total ozone from seasonal to decadal time  
1510 scales, *Atmos. Chem. Phys.*, 11, 11221-11235, <https://doi.org/10.5194/acp-11-11221-2011>,  
1511 2011.  
1512  
1513 Weber, M., Coldewey-Egbers, M., Fioletov, V. E., Frith, S. M., Wild, J. D., Burrows, J. P.,  
1514 Long, C. S., and Loyola, D.: Total ozone trends from 1979 to 2016 derived from five merged  
1515 observational datasets – the emergence into ozone recovery, *Atmos. Chem. Phys.*, 18, 2097–  
1516 2117, <https://doi.org/10.5194/acp-18-2097-2018>, 2018.  
1517  
1518 Wespes, C., D. Hurtmans, L.K. Emmons, S. Safieddine, C. Clerbaux, D.P. Edwards, and P.-F.  
1519 Coheur: Ozone variability in the troposphere and the stratosphere from the first six years of IASI  
1520 observations (2008-2013), *Atmos. Chem. Phys.*, 16, 5721-5743, 2016.  
1521  
1522 Wespes, C., D. Hurtmans, C. Clerbaux, and P.-F. Coheur: O<sub>3</sub> variability in the troposphere as  
1523 observed by IASI over 2008–2016 — Contribution of atmospheric chemistry and dynamics, *J.*  
1524 *Geophys. Res. Atmos.*, 122, 2429–2451, doi:10.1002/2016JD025875, 2017.  
1525  
1526 Wespes, C., Hurtmans, D., Clerbaux, C., Boynard, A., and Coheur, P.-F.: Decrease in  
1527 tropospheric O<sub>3</sub> levels in the Northern Hemisphere observed by IASI, *Atmos. Chem. Phys.*, 18,  
1528 6867–6885, <https://doi.org/10.5194/acp-18-6867-2018>, 2018.  
1529  
1530 Witte, J. C., M.R. Schoeberl, A.R. Douglass, and A.M. Thompson: The Quasi-biennial  
1531 Oscillation and annual variations in tropical ozone from SHADOZ and HALOE, *Atmos. Chem.*  
1532 *Phys.*, 8, 3929–3936, 2008.  
1533  
1534 World Meteorological Organization (WMO): Scientific Assessment of Ozone Depletion: 2006,  
1535 Global Ozone Research and Monitoring Project, Report No. 50, Geneva, Switzerland, 2007.  
1536

1537 World Meteorological Organization (WMO): Scientific Assessment of Ozone Depletion: 2010,  
1538 Global Ozone Research and Monitoring Project, Report No. 52, Geneva, Switzerland, 2011.  
1539  
1540 World Meteorological Organization (WMO): Scientific Assessment of Ozone Depletion: 2014,  
1541 Global Ozone Research and Monitoring Project, Report No. 55, Geneva, Switzerland, 2014.  
1542  
1543 World Meteorological Organization (WMO): Scientific Assessment of Ozone Depletion: 2018,  
1544 Global Ozone Research and Monitoring Project, Report No. 58, Geneva, Switzerland, 2018.  
1545  
1546 Wohltmann, I., R. Lehmann, M. Rex, D. Brunner, and J. A. Maeder: A process-oriented  
1547 regression model for column ozone, *J. Geophys. Res.*, *112*, D12304, doi:10.1029/2006JD007573,  
1548 2007.  
1549  
1550 Yang, E.-S., D. M. Cunnold, M. J. Newchurch, R. J. Salawitch, M. P. McCormick, J. M. Russell  
1551 III, J. M. Zawodny, S. J. Oltmans: First stage of Antarctic ozone recovery. *J. Geophys. Res.* *113*,  
1552 D20308, doi:10.1029/2007JD009675, 2008.  
1553  
1554 Zerefos, C. S., Tourpali, K., Bojkov, R., Balis, D., Rognerund, B., and Isaksen, I.: Solar activity  
1555 – total ozone relationships: observations and model studies with heterogeneous chemistry, *J.*  
1556 *Geophys. Res.*, *102*, 1561–1569, 1997.  
1557  
1558 Ziemke, J. R., A.R. Douglass, L.D. Oman, S.E. Strahan, and B.N. Duncan: Tropospheric ozone  
1559 variability in the tropics from ENSO to MJO and shorter timescales, *Atmos. Chem. Phys.*, *15*,  
1560 8037–8049, 2015.